CHAPTER 4 GAMMA-RAY SPECTRA ANALYSIS

4.1 Introduction

Radionuclides are found naturally in air, water, soil, plants and even human beings are radioactive. In the Earth crust, radioactivity is mainly incorporated in mineral crystals present in rocks or detrital sediments. Their radionuclide concentrations depend on the mineral properties and their origins. For geophysical studies, the heat produced by radioactive decay in rocks is of fundamental importance in understanding the thermal history of the Earth and interpreting amongst others the continental heat-flux data (Chiozzi *et al.*, 2000). The measurement of radionuclide concentrations is an alternative tool to explore the properties of geological structures.

A possible method to explore and study radioactive materials in geological structures is the gamma-ray spectrometry. *In situ* gamma-ray spectrometry is used to provide information on the presence of (radio)nuclides in the environment. In comparison with the sample-collection procedure and subsequent laboratory-analysis, *in situ* measurements are non-invasive, cover an area with more data points, are usually less expensive and are more sensitive with the same precision obtained in a shorter time (Van Wijngaarden *et al.*, 2002a & b). Furthermore, it provides a means to assess the measurements in real time, thus providing the user with locations of interest during measurements. This feature leads to in-field optimisation.

Irradiation of materials with neutrons and the detection of induced gamma-rays have emerged as an attractive instrument for identification and determination of elemental concentrations (Molnár *et al.*, 2000; Nair *et al.*, 2004). The energies of the gamma-rays are characteristic for the isotopes of the elements and their intensities are proportional to their concentrations (Grau and Schweitzer, 1987; Grau and Schweitzer, 1989; Dokhale *et al.*, 2001; Nair *et al.*, 2004). As discussed earlier in section 2.4, fast neutrons (E_n ~14 MeV) emitted by the NuPulse instrument will interact with nuclei of the material surrounding the instrument. Gamma-rays are produced as a result of these interactions mainly following inelastic scattering and neutron-capture reactions. In inelastic scattering reactions, the nucleus is excited to states that are unstable and will usually release the excess energy to reach the ground state by emitting one or more gamma-rays. For the nucleus that has reached the ground state, the sum of the kinetic energy of the exit neutron, target nucleus and the total gamma-ray energy emitted is equal to the kinetic energy of the incident neutron, see also figure 2.2.

Materials containing carbon and oxygen are straightforwardly determined by their characteristic gamma-rays emitted in an inelastic scattering reaction. As fast neutrons (E_n ~ 14 MeV) interact with matter, they also loose energy in elastic scattering (or being moderated) until they reach thermal energies (E_n ~ 0.025 eV). Thermal neutrons excite nuclei by capture reactions (see reaction example in eq. 2.5, ${}^1n + {}^1H \rightarrow {}^2H + \gamma$), leading to an excited state, which decays by characteristic gamma-rays. These capture gamma-rays are emitted by many elements some of which de-excite almost immediately (e.g. H, Si, Fe and Cl) and others have significantly longer half-lives, hence resulting in delayed gamma-ray activities (e.g. Na, Mg, etc).

Both the inelastic scattering and capture gamma-rays are being detected by a gamma-ray detector and, for the NuPulse instrument, the resulting spectra are used to obtain the concentrations of elements. Improvements in the quantitative analysis of

gamma-ray spectra came after the introduction of NaI(Tl) detectors in about 1948 (Debertin and Helmer, 1988; Knoll, 2000). Since then other gamma-ray detectors were developed with specific characteristics and amongst them bismuth germanate (BGO). Both NaI(Tl) and BGO are inorganic scintillating materials with various capabilities in gamma-ray spectroscopy, see more descriptions in section 3.7.3. In the EU-NuPulse project, the RuG/KVI team was commissioned amongst other tasks in charge of calibration and test of the NuPulse instrument that incorporated the BGO detectors system for gamma-ray experiments. The assembled NuPulse instrument that included the BGO (see section 3.7.3 for details) detector was energy calibrated and tested in the test facilities as described in section 3.9.

4.2 BGO detector tests and calibrations

Prior to gamma-ray spectrometry measurements, a detector system has to be tested, and energy and efficiency calibrated. Energy calibration is required to establish the relationship between the channel number of a multi-channel analyser (MCA) and the corresponding gamma-ray energy. Energy calibration will in a later stage help to identify radionuclides by their characteristic gamma-ray energies. The general description of the BGO detector and its associated electronics and data handling and analysis has been described in chapter 3. In this section we focus on the energy and efficiency calibration of the BGO detector.

4.2.1 Energy calibration and energy resolution

To facilitate an energy and efficiency calibration, the NuPulse BGO-detector system was first tested in the laboratory to validate the specifications by the manufacturer. The detector system was placed in a low-level activity counting system, being a 10 cm thick low-activity lead castle (see section 3.7.3 on HPGe system). The lead-castle facility reduces the contributions from all other materials, e.g. cosmic rays and building materials. Figure 4.1 shows the gamma-ray spectrum for the initial tests and energy calibrations within the lead castle involving the use of standard gamma-ray sources, a) ^{137}Cs; b) ^{40}K; c) ^{60}Co and d) monazite for ^{232}Th. The gamma-ray spectra shown in figure 4.1 for the given standard gamma-ray sources cover a combined energy range of E_γ = 0.2 - 2.7 MeV.

Radionuclides such as ^{137}Cs and ^{40}K emit mono-energetic photons, while ^{60}Co decays by emission of two gamma-rays (E_γ = 1.17 & 1.33 MeV). The two gamma-rays stemming from the ^{60}Co source appear as a double-humped peak in figure 4.1 (c) since the energy resolution of the NuPulse BGO detector is insufficient to resolve them. In the ^{40}K and ^{60}Co spectra one notices the E_γ = 2.61 MeV from the ^{208}Bi (see also figure 4.4) in the BGO crystal. The spectra in figure 4.1 were taken with acquisition times ranging between 500 s and 5000 s. The count rate in figure 4.1 d) is presented on a logarithmic scale to better distinguish the various components since the intensity of the spectrum covers three orders of magnitude.

To determine the energy-calibration factors for the detector, the peak energies associated with the standard gamma-ray sources (used in figure 4.1) were plotted against the centroid channel number as presented in figure 4.2. The centroid channel

numbers were derived from the spectra in Figure 4.1. The linear fit in figure 4.2 gives a good description of the measured data as one can observe from the value of the reduced chi-squared ($\chi^2 = 1.17$). From these results it can be concluded that the response of the NuPulse BGO-detector system is linear in photon energy up to 3 MeV**.** As follows from figure 4.1, the detector and its associated electronics have an offset of E = 60 keV. For NuPulse field tests, photon energies above E_γ = 3 MeV are expected but standard sources to match the high energies are unavailable. Until we find counter evidence, a continuation of the linear relation between channel number and gamma-ray energy will be assumed.

Because the light output of BGO crystals decreases with increasing temperature, the proportionality of channel number and energy scale for such crystals can be accomplished only within a period of constant temperature. Figure 3.11 showed the dependence of the scintillation signal on temperature for a BGO detector and for other detectors. It was assumed that the temperature in the laboratory was constant during all the measurements. Regular energy calibrations will be required for the NuPulse field experiments as temperature variations are expected, hence gain-drift corrections become essential.

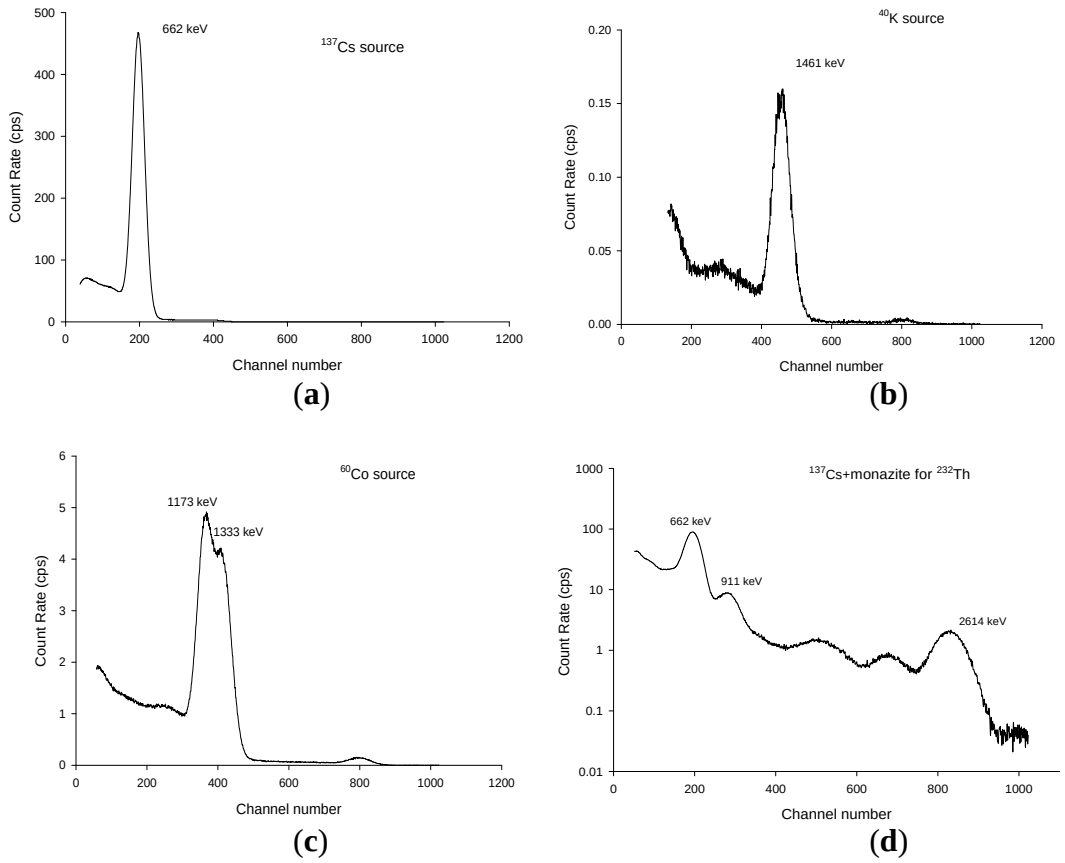

Figure 4.1: *Gamma-ray spectra averaging the count rate per channel measured with the BGO detector for the standard sources; a) ^{137}Cs, b) ^{40}K, c) ^{60}Co and d) ^{137}Cs+monazite for ^{232}Th. Please note that part d) is presented with a logarithmic vertical scale.*

The follow-up test measurements focused on the energy resolution of the BGO detector. Energy resolution is the ability of the detector to resolve two peaks that are close together in energy or an ability to distribute pulses of incoming radiation around an average pulse height (H_0). The relative energy resolution of a detector, R, is therefore defined as the full width at half maximum (*FWHM*), divided by the location of centroid channel of the photopeak, H_0 (Knoll, 2000). The energy resolution, R, is a dimensionless number conventionally expressed as a percentage; the lower the value, the better is the energy resolution:

$$R = \frac{FWHM}{H_0} \times 100\%. \qquad (4.1)$$

The FWHM is defined as the width of the distribution at a level that is just half the maximum value of the peak over background. The resolution was calculated for the full energy peaks of ^{137}Cs, ^{40}K, ^{208}Tl and the sum full energy peak of ^{60}Co. The E_γ = 1173 and 1333 keV full energy peaks were excluded because as shown in figure 4.1c, this detector could not separate these peaks. Table 4.1 contains the resolution measurements data and the specified value provided by the detector manufacturer. In addition to table 4.1, the resolution is plotted as a function of energy in figure 4.3. The figure includes the resolution specified by the manufacturer and is represented by a solid circle at energy E_γ = 662 keV. The uncertainties in the resolution values are estimated from fluctuations in the FWHM values obtained for slightly different regions of interest. It can be concluded that the measured resolution at E_γ = 662 keV is, within the uncertainty, in agreement with the specification given by SCIONIX.

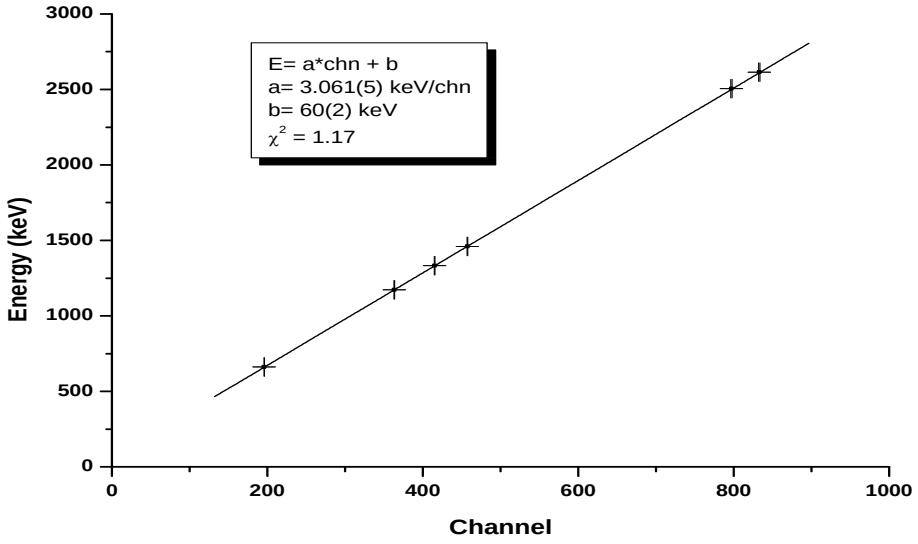

Figure 4.2: *Peak energy as a function of channel numbers.*

Table 4.1: *The resolution measurement results for the gamma-ray standard sources, ^{137}Cs, ^{60}Co, ^{40}K and ^{208}Tl for the BGO detector.*

Centroid (channel)	Nuclide	E_γ (keV)	KVI, R (%)	SCIONIX, R (%)
195.9 ± 0.2	^{137}Cs	662	17.9 ± 1.8	16.3
363.3 ± 0.4	^{60}Co	1173	-	
415.2 ± 0.5	^{60}Co	1333	-	
457.5 ± 0.5	^{40}K	1461	11.7 ± 0.9	
797.1 ± 0.8	^{60}Co sum peak	2506	8.8 ± 0.6	
832.8 ± 0.8	^{208}Tl	2614	9.3 ± 0.6	

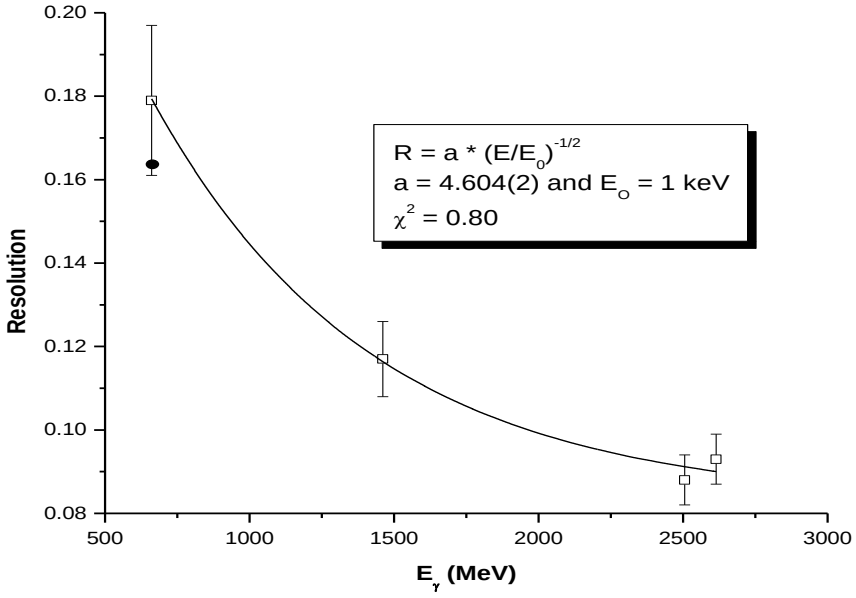

Figure 4.3: *Energy resolution as a function of energy.*

4.2.2 Intrinsic radioactivity

Next, the gamma-ray background contribution from the detector materials was assessed. To achieve proper statistics, the BGO intrinsic background spectrum was acquired over t = 252000 s (70 hours) with the detector placed inside a lead-castle. The resulting spectrum is presented in figure 4.4. This low-activity counting system is located inside the KVI building, thus it was assumed that for the duration of the measurement, the room temperature remained constant.

The background radiation spectrum in the energy range of E_γ = 0.2 – 3.0 MeV shown in figure 4.4 arises from radionuclides present in the BGO crystal, the PMT (photomultiplier tube), cosmic rays and from materials emitting high-energy gamma-rays outside the lead castle, which are not fully absorbed by the castle. For the NuPulse BGO detector, the PMT is equipped with a low-K glass to reduce the ^{40}K-

background contribution (SCIONIX). A contribution from the PMT (stemming from ^{40}K (E_γ = 1461 keV)) is therefore small as no clear evidence is observed in the spectrum. The gamma-ray spectrum in figure 4.4 shows the contributions of ^{207}Bi (E_γ = 570, 1063 and 1633 keV (coincidence summing peak)) and ^{208}Bi (E_γ = 2614 keV) from the detector-system. The bismuth isotopes are found in the detector crystal and originate from the nuclear reactions of cosmic charged particles with stable lead isotopes in the ore, from which the BGO crystal is grown (Lewis, 1988). In addition, external radiation from the decay of ^{232}Th in the building materials may contribute to the E_γ = 2614 keV peak. No other contributions due to ^{232}Th-decay were observed hence it was assumed that the contribution to the E_γ = 2614 keV peak from ^{232}Th decay was small compared to the ^{208}Bi contribution.

The gamma-ray spectrum presented in figure 4.4 serves as the detector background spectrum that is an integral part of the spectrum analysis in measurements with this detector system. For the present NuPulse work, the background spectrum in figure 4.4 is found to be only a minor component to the *in situ* spectra.

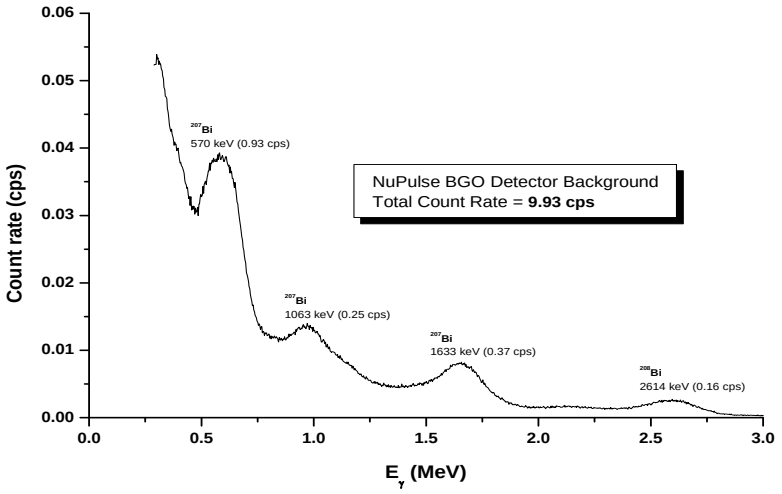

Figure 4.4: *Intrinsic gamma-ray background spectrum of the NuPulse BGO detector system. The peaks are labelled with their energy and the nucleus from which they originate.*

4.3 Efficiency calibrations in the test facilities

After verifications and calibrations of the NuPulse BGO detector, the next step was to test the instrument for field-type experiments. The NuPulse instrument was deployed at experimental facilities available at the KVI for these tests. The facilities at the KVI include a 3 m high concrete tank (10 cm thick walls) with 2 m inner diameter (shown in figure 3.16 of section 3.9.2) and a borehole described in section 3.9.3. Measurements in these facilities are carried out using two experimental modes, the neutron generator-off (PNDT-off) and neutron generator-on (PNDT-on) modes.

4.3.1 Concrete tank experiments for PNDT-off

Without neutron generator, the assembled NuPulse instrument equipped with BGO gamma-ray detector system was placed inside the concrete tank. In this PNDT-off assembly, the BGO detector crystal is positioned about 20 cm from the bottom surface of the tank. In the first test, the tank was left empty with only the NuPulse instrument present and the gamma-ray spectrum "empty spectrum" was acquired.

In the follow-up experiment, the tank was filled with water and a second gamma-ray spectrum, the "water spectrum" was acquired. Both gamma-ray spectra are presented in figure 4.5, with the intensities presented on a logarithmic scale. At energies higher than E_γ = 3 MeV, both spectra are similar and are dominated by the continuum due to signals induced by cosmic-ray particles in the detector.

In the first setting, the empty-tank spectrum reflects mainly the gamma-rays from the concrete tank walls, cosmic rays and the surface below the tank. The empty-tank spectrum in figure 4.5 shows distinctively the contributions by ^{40}K and the ^{208}Tl from the ^{232}Th-decay series. Moreover, the water-filled tank spectrum for $E_\gamma < 3$ MeV shows an order of magnitude lower count rate compared to the empty-tank spectrum. Water has an almost similar effect of shielding as the lead castle in the experimental test described in section 4.2. The other contribution to the water spectrum was dominated by the fact that the front face of the detector was only about 20 cm from the bottom surface of the tank. This provided enough shielding for cosmic ray particles and less for the bottom surface. The other observation for the two spectra is that the reduction in thorium peak is larger (from empty to water) than the potassium and uranium peaks (U is assumed to give rise to the bump in the region between the ^{40}K and the ^{232}Th peaks). The shoulder on the K peak of the water spectrum and the bump at $E_\gamma \sim 0.6$ MeV arise from the intrinsic radioactivity of the detector set-up. Altogether the water spectrum mainly consists of the contribution from the detector set-up and the soil under the tank, partly shielded by water.

The total count rates for the energy interval E_γ = 0.15 – 3.2 MeV in both spectra, empty-tank and water-filled tank are 124.10 ± 0.11 and 11.589 ± 0.014 cps, respectively. The total count rate in that interval for the water-filled tank spectrum is slightly higher than that of the spectrum measured in the lead castle (9.931 ± 0.006 cps). For further experimental analysis with the PNDT-off in the tank, the water spectrum will serve as background spectrum.

4.3.1.1 The water + KCl solution analysis

Subsequently, various amounts of KCl were mixed with water. In the natural environment, as can be seen in figure 4.5 in the empty spectrum, some activity exists due to presence of ^{40}K. In the water-filled tank spectrum, the contribution from ^{40}K was small, due to the shielding by the amount of water surrounding the gamma-ray detector. A mixture of KCl-water solution will enhance the ^{40}K contribution depending on the amount of KCl added. To investigate and observe these spectral changes in real time, KCl was added in steps of 50 kg and a spectrum was acquired for each solution. To ensure that the solution is homogeneous given the size of the tank and the amount of water, an electric motor was deployed to stir the solution for every amount of KCl added. In order to achieve equal experimental conditions, it was essential that both PNDT-off and PNDT-on spectra were acquired in succession. That

implied that after the preparation of each solution, following the PNDT-off measurement the neutron generator was assembled and a PNDT-on spectrum was acquired. Experimental results for the PNDT-on measurements will be discussed in section 4.3.2.

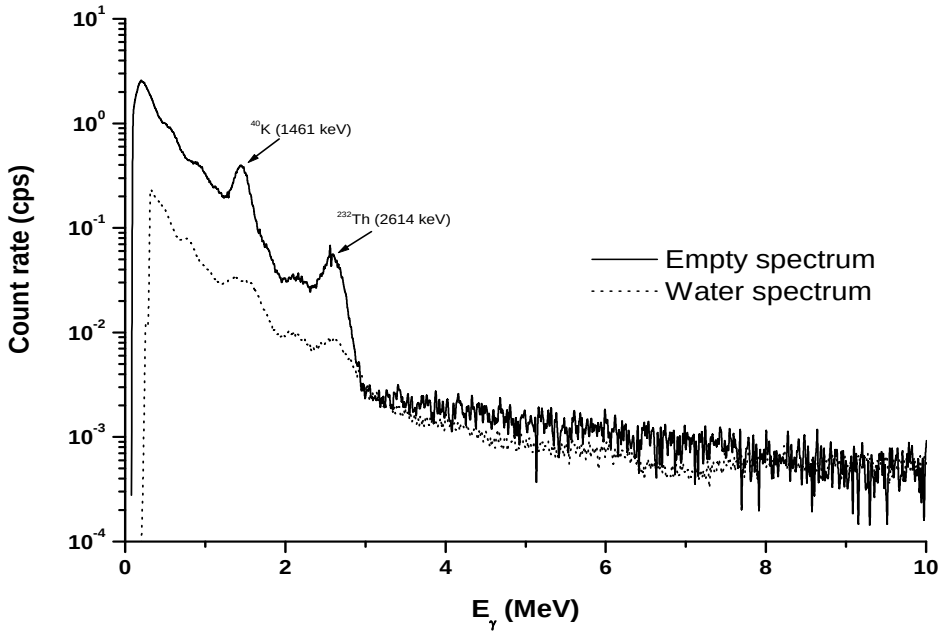

Figure 4.5: *Experimental gamma-ray spectra in the empty and water-filled concrete tank.*

Potassium has a naturally radioactive isotope, ^{40}K, which emits a single gamma-ray at E_γ = 1.46 MeV. Figure 4.6 is presented in two parts showing the background (water sample) spectrum and spectra taken with various amounts of KCl dissolved in water. As more KCl was dissolved to the water, the intensity of the ^{40}K peak in the spectra increased. All the KCl solution spectra were analysed for their potassium content with Full Spectrum Analysis (for FSA see section 3.8.2) including the background spectrum obtained for the water-filled tank. From figure 4.6 one notices that the part of the spectrum for E_γ > 2 MeV is not affected by the KCl concentration.

The activity concentrations derived from the experimental spectra in figure 4.6 were compared to the ones calculated from the added mass of KCl by using the known activity of 1 g of KCl (16.26 ± 0.10 Bq ^{40}K, see intermezzo 4.1) and the amount of water in the tank. The count rates of gamma-ray spectra shown in figure 4.6 for the E_γ = 0.2 – 3 MeV range demonstrate the intensity increase as expected for the ^{40}K full-energy spectrum as the amount of KCl was added. A more detailed explanation on the analysis of the water+KCl solution will follow later in this chapter.

Analyses using the MPA (section 3.8.1) follow the FSA method, which requires that the entire spectrum (including the continuum) be integrated in the analysis. For the water+KCl solution, only the ^{40}K activity concentration is expected which thus gives rise to only one gamma-ray line. For this setting, we investigate the effect of using the full spectrum as compared to the peak-region method. In the peak-

region method, the activity concentration is determined from the net content within the window set around the full energy peak. In an investigative test, similar procedures as in FSA will be followed excluding the continuum.

In figure 4.7, a measured spectrum of the solution (water + 50 kg KCl) is used to test the sensitivity of the analyses if only the region around the peak is considered as compared to the full-spectrum. In both cases shown in figure 4.7, the best fit is based on the minimum reduced χ^2 value. In figure 4.7, the top spectrum shows the results of the analysis for the region in channel 10 to 270. In the bottom spectrum, the area around the full energy peak (channels 40 to 70) is analysed. Regions have been indicated, where the calculated Gaussian shape deviates from the shape of the experimental spectrum.

To a large extent the region selected for the analysis does not affect the activity concentration of ^{40}K as shown in figure 4.7. Furthermore, the background that is mainly due to cosmic rays also stays constant. In the analysis of a single gamma-ray line, the peak-region method gives a reliable value of the activity and allows a close investigation of the parameters involved in the fitting. For example, one is able to monitor the effect of broadening of the peak to which the fit of the entire spectrum may be less sensitive and may even result in unreliable values. The reason for this is that in both cases the best fit to the spectrum follows from the minimum reduced chi-squared values.

In the analysis of the full spectrum, the fit to the continuum may dominate over the fit to the peak area, whereas in the peak-region method the fit to the peak dominates. The possible explanation for the better fit in the full-spectrum is related to the way the reduced chi-squared value is calculated by the MPA. The reduced χ^2 value in the MPA is calculated based on the following expression;

$$\chi^2 = \frac{1}{n-1}\sum_{i=1}^{n}\frac{\left[(S(i)-Bg(i))-\sum_j C_j SS(i)\times L_T\right]^2}{\sigma_i^2} \qquad (4.2)$$

where *S(i)* is the measured spectrum, *Bg(i)* the background spectrum, C_j the activity concentration for a certain radionuclide, *SS(i)* the standard spectra and L_T the live-time of the acquired spectrum, $\sigma_i^2 = \mathrm{var}\big(S(i)-Bg(i)\big) = S(i)+Bg(i)$. The index *i* runs from 1 to *n* and represents the channel numbers. In figure 4.7, for the full-spectrum analysis, the *n*-value (number of channels used) is high. The analysis includes the background spectrum that is not affected by KCl and should on average yield a $\chi^2 \sim 1$. Hence the reduced χ^2 value for the total spectrum is relatively low compared to the value for peak-region method. In the analysis it is assumed that peaks have a Gaussian shape.

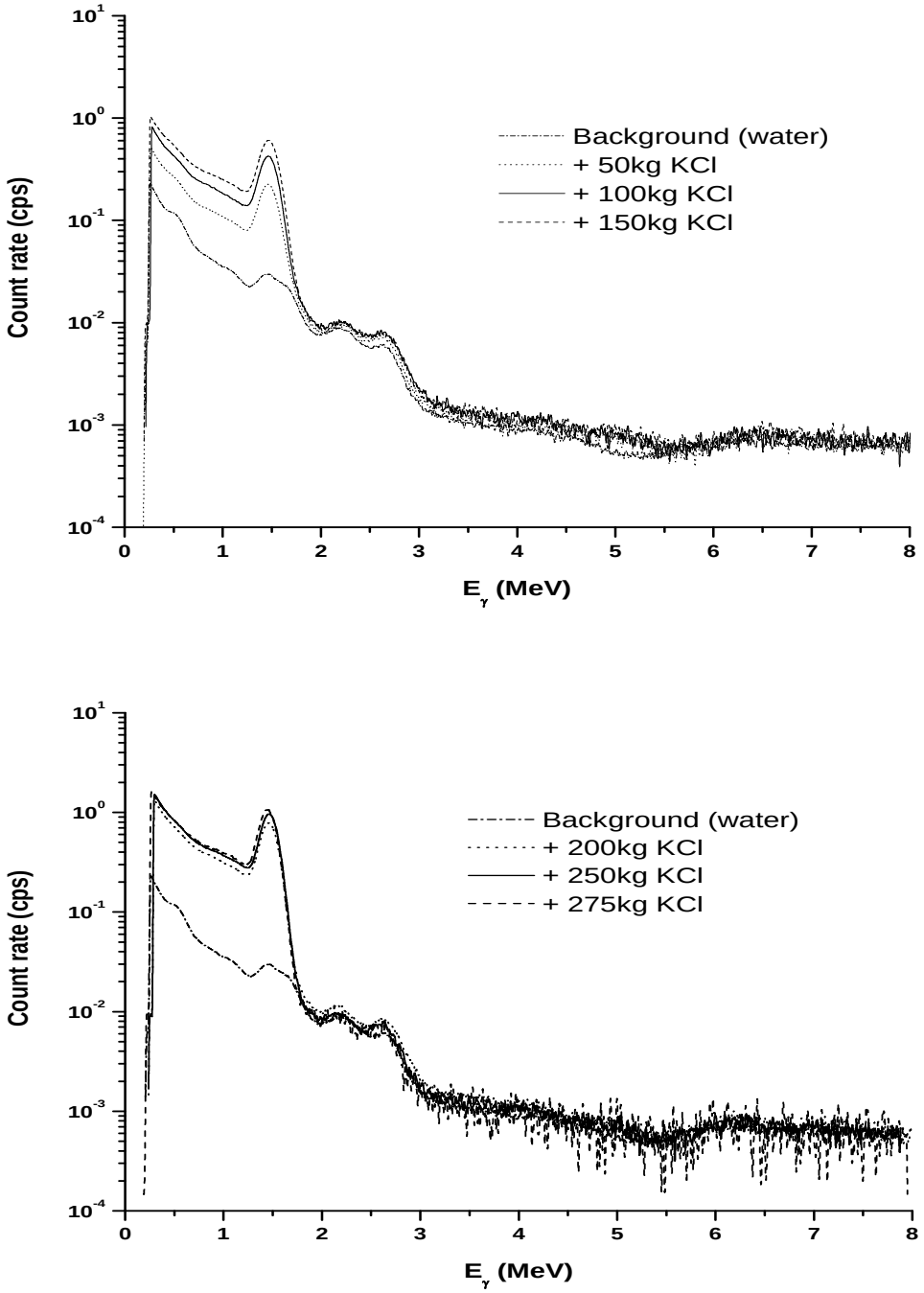

Figure 4.6: *Gamma-ray spectra for water (background) and various amounts of KCl dissolved in water.*

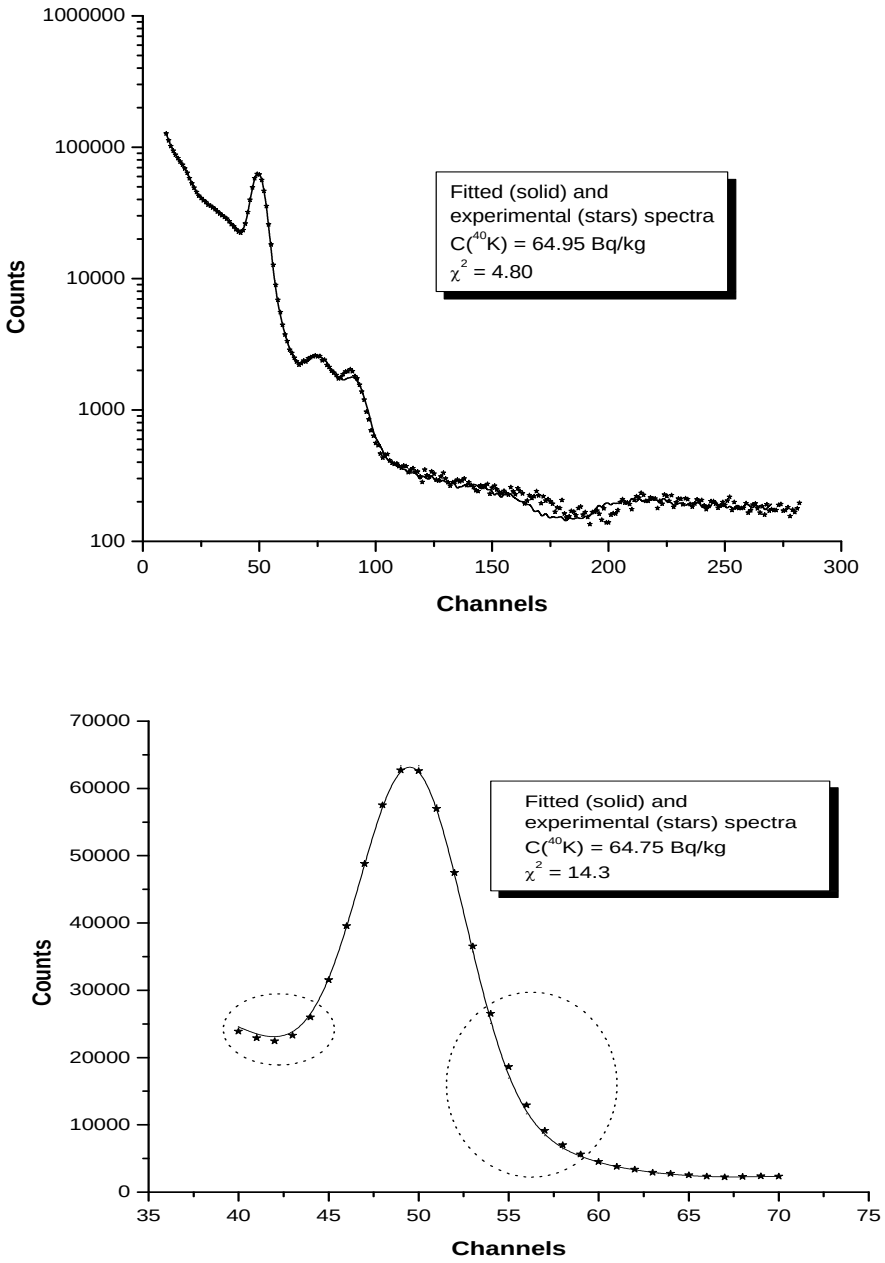

Figure 4.7: *The effect of the cut-off range selection to the activity concentration of the measured sample and the reduced* χ^2 *value. In the bottom part of the figure the regions are indicated where the fitted spectrum deviates from the experimental one. Note that the vertical scale of the top spectrum is logarithmic and linear for the bottom spectrum.*

The resolution of the BGO is relatively low and is affected by the temperature variations. Consequently, the data analysis relied on the measured spectrum rather than on the manufacturer's specifications (see also table 4.1). It was found that the MPA fit analysis was sensitive to the broadening function of the calculated spectrum.

To correctly represent the best broadening function parameters for the MCNPX calculations ($FWHM = a + b\sqrt{E + cE^2}$, parameters *a*, *b* and *c* are specified by the user and *E* is the energy in MeV), for each measured spectrum the FWHM was determined first and then incorporated in the simulations. Given the limitations discussed above, further tests of the peak-region method were explored for various solutions of water + KCl.

In the Monte Carlo calculations (see section 3.8.4), the light collection properties of the detector system are not simulated. The magnitude of simulated standard spectra therefore needs to be compared to a measurement with a known standard source, to determine the efficiency-calibration factor between the simulation and the measured spectrum in a given geometry. With the known amount of KCl added to the water, the activity concentration of the solution can be calculated. With all available information on the detector system, MCNPX simulations standard spectra are generated and used to analyse the measured water + KCl spectra. The efficiency-calibration factor is then derived as the ratio between the activity concentrations of the analysed spectrum and the expected activity concentration of the solution, ($\varepsilon = \frac{C_{Analysed}}{C_{Expected}}$). The uncertainties in the efficiency-calibration factors are calculated using the relation,

$$\sigma(\varepsilon) = \varepsilon \cdot \sqrt{\left(\frac{\sigma(C_{Analysed})}{C_{Analysed}}\right)^2 \times \chi^2 + \left(\frac{\sigma(C_{Expected})}{C_{Expected}}\right)^2}, \qquad (4.3)$$

where $\sigma(C)$ represents the combined statistical and systematic uncertainties in the analysed and expected spectrum. The multiplication by χ^2 accounts for systematic deviations in the analysed spectra. The reduced χ^2–value represents the goodness of fit between the measured and the calculated spectra for the peak-region method. The $\sigma(C_{Expected})$ contains systematic uncertainties due to the experimental set-up, i.e. the uncertainty due to the tank radius estimated as 100.0 ± 0.5 cm, height as 210 ± 1 cm and 0.5 kg for each 50 kg bag of KCl. The rationale behind the inclusion of the systematic uncertainties is that each systematic uncertainty may have a well-defined but unknown direction (either + or -), so in total they are likely to behave as a statistical uncertainty.

Table 4.2 lists the expected and analysed concentrations of ^{40}K and the derived calibration factors, ε. From table 4.2 it is clear that, as the mass of KCl increases or the intensity of the ^{40}K peak increases, the fit deteriorates as shown by the increased values of the reduced χ^2. Since the measurements were conducted outdoors and over several days, the temperature variations could affect the gain drifts of the BGO detector. The increased reduced χ^2 values thus indicate that, as more KCl was added, the systematic uncertainties in the spectra start to dominate over the statistical uncertainties.

In figure 4.8 (see also figure 4.7), the water+KCl solutions with 50 kg and 275 kg of added KCl are inspected. The upper panel is for the 50 kg and the fit looks much better with a lower reduced χ^2 value. In the bottom panel (275 kg), although the fit appears satisfactory, the reduced χ^2 value is four times higher. For the bottom panel one notices that the calculated data on the low and high-energy side of the peak are

slightly higher than the measured data. These deviations indicate that the measured peaks are not fully described by Gaussian shape and hence such an effect cannot be remedied by adjusting the Gaussian broadening. Again, the small variations in the fit to the data show that the MPA is extremely sensitive to small changes in the shape of the spectra and one has to take extra care to correctly represent the analysed data.

The results presented in table 4.2 show that the calibration factor is independent of the KCl concentration. The weighted efficiency average, $\varepsilon = 0.537 \pm 0.015$ (with $\chi^2 = 1.18$) indicates that about 54% of expected pulses are recorded.

Table 4.2: *Activity concentration (Bq kg^{-1}) for the ^{40}K in the concrete tank. The uncertainties in the analysed data represent the external uncertainties.*

KCl mass (kg)	Expected activity conc. (Bq kg^{-1})	Analysed activity conc. (Bq kg^{-1})	χ^2	ε
50	123.2 ± 1.5	67 ± 8	3.4	0.54 ± 0.07
100	246 ± 2	132 ± 12	10.55	0.54 ± 0.05
150	370 ± 3	196 ± 14	11.6	0.53 ± 0.04
200	493 ± 4	264 ± 17	64	0.53 ± 0.03
250	616 ± 5	333 ± 18	210	0.54 ± 0.03
275	678 ± 5	365 ± 19	226	0.54 ± 0.03

To further verify the ε-values obtained, the 'hybrid' method (see section 3.8.3) was deployed to analyse the spectra. Each spectrum was divided into four regions as shown in figure 4.9 (similar to figure 3.12). A few spectra shown in figure 4.6 are chosen and presented in figure 4.9 to demonstrate the regions of interest. In each region, the total count rate was determined and presented in table 4.3. Table 4.3 also includes the weighted-average count rates for the three regions (**I**, **II** and **III**) and their reduced χ^2 values. From the results presented in table 4.3, in those three regions, cosmic (**I**), thorium (**II**) and uranium (**III**), the total count rates do not vary much from one concentration to another. This is consistent with the statement made in the discussion of figure 4.6 that the count rates for energies $E_\gamma > 2$ MeV were not affected by the addition of KCl in water.

As expected, the addition of KCl in water mainly affected the count rates in the potassium region (**IV**). To check the high χ^2 values reported in table 4.3, also the sum of the first three regions is combined with the weighted average and the reduced χ^2 value. The results of this operation show that the precise settings of the intervals do not contribute to the high χ^2 values reported for each region. Moreover, the χ^2 values are approximately the same for all the intervals hence indicating no evidence of dominant and varying radon concentration in the water tank. Also here the high χ^2 values indicate that systematic uncertainties (e.g. assumption of constant background) dominate over the statistical ones. As indicated in table 4.3, the (cosmic) background varies by about ± 10%. In principle, corrections for variations in background could be made, but were omitted because they would stretch the precision beyond the purpose of this experiment.

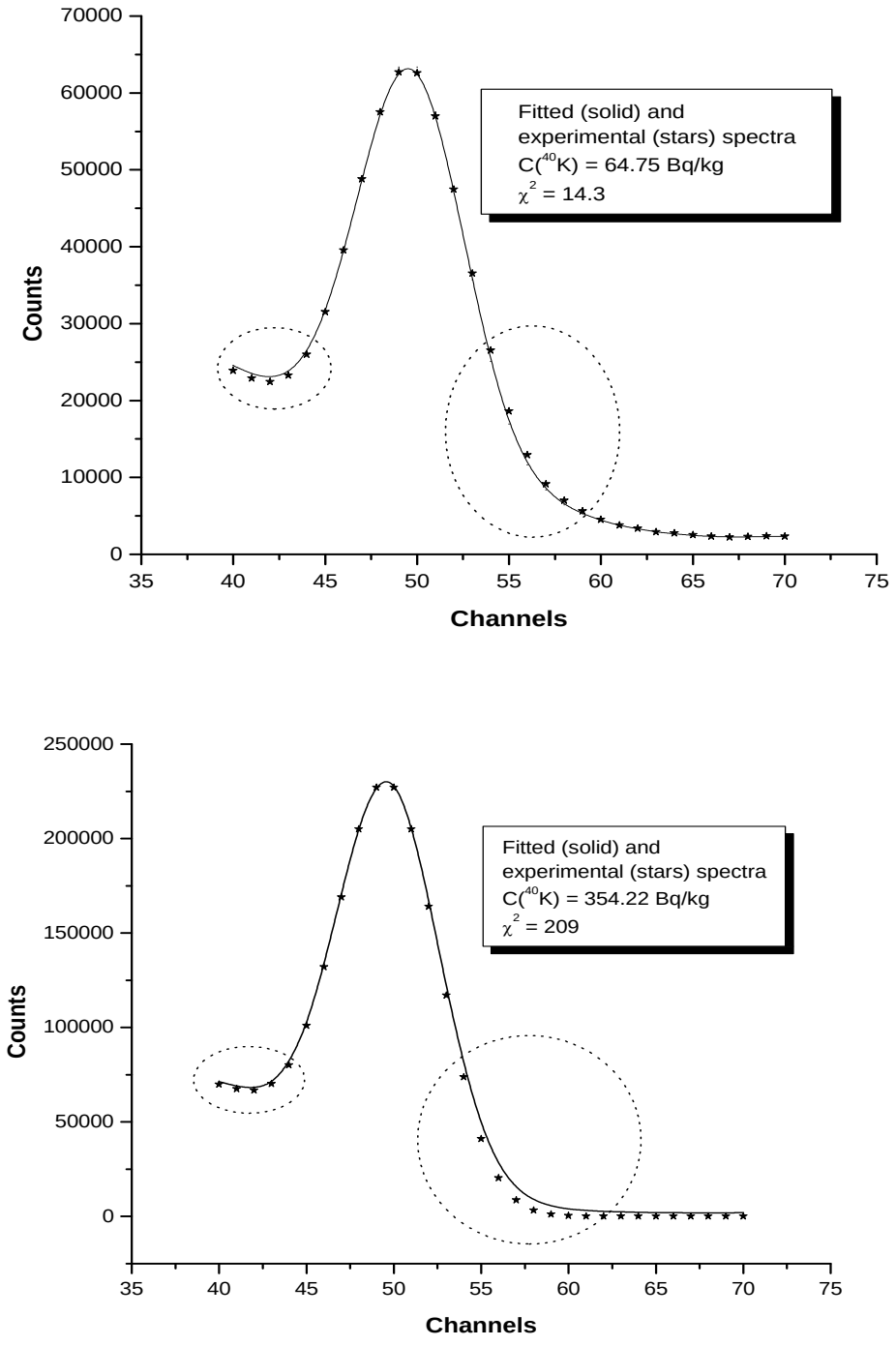

Figure 4.8: *Two spectra showing the effect on the reduced* χ^2 *value as the activity concentration increases (i.e. statistical uncertainty decreases) for tank solutions with 50kg KCl (top) and 275 kg KCl (bottom) added. In the figure the regions are indicated where the fitted spectrum deviates from the experimental one.*

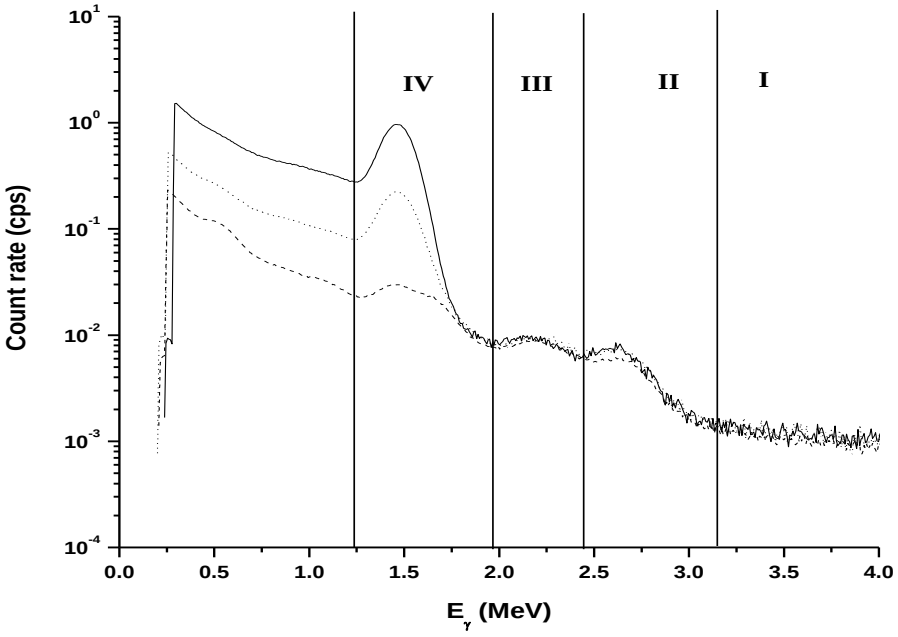

Figure 4.9: *Gamma-ray spectra for the background and for some selected amounts of KCl dissolved in the water tank (c.f. fig. 4.6).*

Table 4.3: *Total count rates (in cps) in the given regions for various amounts of KCl dissolved in water. The weighted average count rates and their external uncertainties together with the reduced* χ^2 *values are included.*

Conditions	**I**	**II**	**III**	**IV**	**Sum (I + II + III)**
Background	0.4532 (14)	0.4150 (13)	0.4690 (14)	2.209 (3)	1.337 (2)
50kg KCl	0.476 (3)	0.363 (2)	0.463 (3)	8.251 (10)	1.302 (4)
100kg KCl	0.517 (3)	0.411 (3)	0.510 (3)	14.481 (17)	1.438 (5)
150kg KCl	0.542 (3)	0.399 (3)	0.497 (3)	20.038 (19)	1.438 (5)
200kg KCl	0.497 (3)	0.436 (3)	0.560 (3)	26.135 (19)	1.493 (5)
250kg KCl	0.464 (3)	0.382 (3)	0.501 (3)	32.02 (2)	1.347 (5)
275kg KCl	0.451 (8)	0.335 (7)	0.465 (8)	34.24 (7)	1.252 (13)
Weighted average	0.476 (12)	0.4027 (10)	0.4875 (12)		1.37 (3)
χ^2	166	130	174		274

In figure 4.10, the total count rates of the potassium region are plotted against the added mass of KCl. The background spectrum was considered to have 0 kg of KCl. The data were fitted with a linear function as shown in figure 4.10 and the result shows that adding 1 kg KCl to the tank increases the count rate by (0.11959 ± 0.16) x 10^{-3} cps in this region (**IV**). Adding 2.46 Bq per l ^{40}K (see intermezzo 4.1) increases

the count rate by 0.11959 cps, thus the count rate per Bq is ($\frac{0.11959}{2.46}$) = (0.04853 ± 0.7) x 10^{-4} cps/Bq.

The MCNPX simulated standard spectrum (1 Bq per l_{H_2O}) for the potassium region was found to be 0.0914 cps. Thus the detector efficiency is calculated as:

$$\varepsilon_{det} = \frac{0.04853}{0.09143} = 0.531 \pm 0.008$$

The above efficiency factor agrees within uncertainties with the previous efficiency calibration factor ($\varepsilon = 0.537 \pm 0.015$) determined using the MPA method to analyse the spectra. The above results showed that the NuPulse BGO detector system has an efficiency of about 54%. This calibration factor is valid for a given BGO detector system and in principle is an intrinsic property, independent of the geometry.

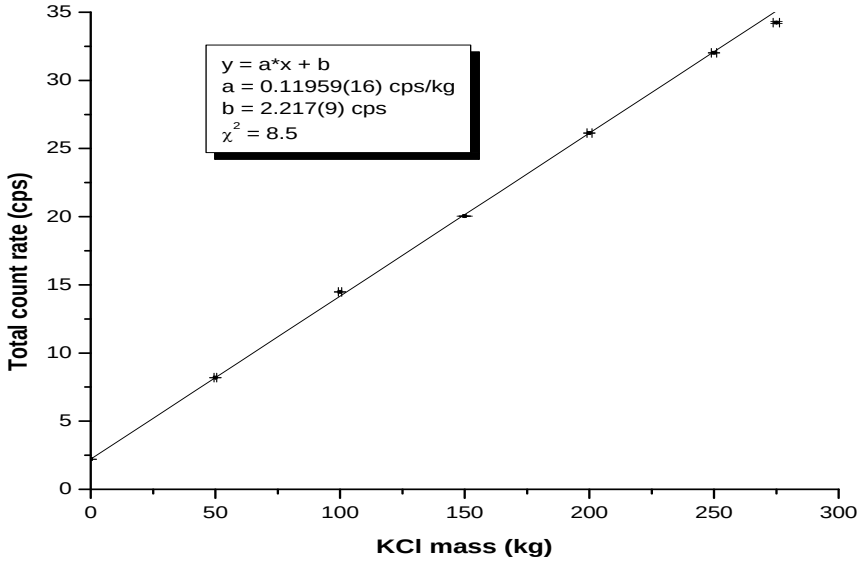

Figure 4.10: *Linear fit to the data of total count rate in the potassium region against the dissolved mass of KCl in the water. The uncertainties in the fit parameters represent the external uncertainties.*

Intermezzo 4.1: <u>The relation between mass and activity of KCl</u>.

- The number of moles in 1kg KCl are determined as:
$$\frac{KCl_{mass}(g)}{KCl_{molar-mass}(g \cdot mol^{-1})} = \frac{1000\,g}{74.551 g \cdot mol^{-1}} = \mathbf{13.41}\ \text{mol of KCl.}$$

- 13.4 mol KCl is equivalent to about **8.08 x 10^{24}** atoms of KCl and thus **8.08 x 10^{24}** nuclei of K.
- For each nucleus of K, 0.0117 % are ^{40}K. This implies that 13.4 mol KCl contains 8.08 x 10^{24} x 1.17 x10^{-4} = **9.45 x 10^{20}** nuclei of ^{40}K.
- $Activity = \lambda \cdot N = \frac{\ln 2}{t_{1/2}} \cdot N$. With $t_{1/2}$ (^{40}K) = (**1.277 ± 0.008) x 10^{9}** years (Firestone, 1996) and the above number of ^{40}K nuclei, the activity was calculated to be **(1.626 ± 0.010) x 10^{4}** Bq,

- The volume of the water in the tank = **6600 ± 90** *l* and is equivalent to about 6.6 x 10^{3} kg of water.

- Thus adding 1kg KCl to the tank, the concentration increased by $(\frac{1.6\times10^{4}\,Bq}{6.6\times10^{3}\,l_{H_2O}})$ = **2.46 ± 0.04** Bq ^{40}K per l_{H_2O}.

4.3.1.2 The borehole formation analysis tests

Additional PNDT-off experiments involved the NuPulse instrument being deployed in the borehole drilled in front of the KVI building, see section 3.9.3 for details about the KVI borehole. The instrument was lowered to the bottom of the borehole and gamma-ray spectra were acquired for each 1 or 2 m step upwards. The step-size was associated with the specification of the borehole formation as discussed in section 3.9.3. In the water-tank experiment, the activity concentrations of ^{40}K were known beforehand and hence the peak-region method was used. For the borehole experiments, the three naturally occurring radionuclides (^{40}K, ^{232}Th and ^{238}U) are of interest with varying activity concentrations.

As an initial test, sets of new standard spectra for the borehole geometry were simulated with MCNPX. The purpose of the new standard spectra was first to analyse the borehole-measured spectra and compare the activities to the values in HPGe analysed samples (described in section 3.7.3). We assume the borehole formation, consisting of a homogeneous mixture of quartz sand (SiO_2, density 2.65 g cm^{-3}) and fresh water (H_2O, density 1.00 g cm^{-3}) is modelled with a bulk density[4] of 2.16 g cm^{-3}. Furthermore, we assume that the gamma-radiation is only emitted by the formation and not by casings, detector or the borehole fluid. For more details about simulation specifications, see appendix C. We will use 50 cm as our infinite thickness for the source specification in agreement with Hendriks, (2003).

[4] SiO_2 with porosity (ε) of 30% and all the pores saturated with H_2O.

In addition, the 'hybrid' method will also be implemented to the borehole spectra analysis. A window was set in the spectrum (normalised to the measuring time) over the major peaks of each radionuclide of interest: E_γ = 1.46 MeV for ^{40}K, E_γ = 1.76 MeV for ^{238}U (indirectly from ^{214}Bi) and E_γ = 2.61 MeV for ^{232}Th (indirectly from ^{208}Tl).

At the time of the drilling (in 1999), samples were collected at various depths of the borehole and analysed on the available HPGe gamma-ray detector system at the KVI. All samples collected were dried first and sealed for a period of about 4 weeks prior to the measurement in the HPGe detector system. For the determination of the ^{238}U activity concentrations, daughter radionuclides (^{214}Bi and ^{214}Pb) are used, hence the system should be in secular equilibrium. In the decay series of ^{238}U, the radon (^{222}Rn) gas may escape from the system and thus no secular equilibrium can be guaranteed. Thus the samples are sealed such that no radon gas escapes. ^{222}Rn has a half-life time of about 3.8 days and a period of 4 weeks means that about 99% of ^{222}Rn have decayed and secular equilibrium is restored.

The average sample mass measured at the HPGe system was about 500 g. The samples would provide estimates for the activity concentrations at various depths (or formations) of the borehole. According to borehole sample records, each sample was taken and labelled to represent a range in the borehole of about one metre. Comparable to the NuPulse instrument, the HPGe analysed sample would be limited as the NuPulse instrument would be exposed to massive formation as seen by the detector module. Moreover, the borehole water closer to the detector may contain radon, thereby contributing to enhanced 'effective' concentrations of uranium in the NuPulse instrument measurement.

The activity concentrations derived from the spectra measured with the NuPulse instrument in the KVI borehole are presented in figures 4.11 to 4.13 as a function of depth and are compared to the values obtained from the sample analysis on the HPGe detector. Also in figures 4.11 to 4.13, the subdivisions of the formation types surrounding the borehole. The activity concentrations are in good agreement for ^{238}U and ^{232}Th for the two sets of measurements. For our ^{40}K data, there is a systematic deviation from the HPGe data being about 25% higher than NuPulse (mainly in Westland 1 formation). The reason is not yet understood. The HPGe results are based mainly on dried and small Marinelli-beaker samples and for the NuPulse instrument the large volume of the borehole formation is the source. Besides, this outcome does not explain why the ^{238}U and ^{232}Th concentrations are in good agreement and ^{40}K not. The FSA was investigated for potentially causing the deviation for ^{40}K, but the 'hybrid' method gives similar results

The results of figures 4.11 to 4.13 are summarised in table 4.4. The activity concentrations (weighted average) for the given formation are presented for both the HPGe and NuPulse-instrument systems. From table 4.4, it is noticed that the corresponding values for NuPulse and HPGe analyses agree well and show similar variations with the soil formations, indicating that each formation has its own radiometric fingerprint.

Table 4.4: *Activity concentrations (Bq/kg) for radionuclides in the borehole experiment for various soil formations in both the HPGe detector system and the NuPulse instrument.*

Formation	**Westland 2**	**Westland 1**	**Eem**	**Peelo**
^{40}K (HPGe)	521 ± 19	362 ± 7	301 ± 9	230 ± 10
^{40}K (NuPulse)	484 ± 4	255.3 ± 1.8	251.9 ± 1.8	178 ± 3
^{238}U (HPGe)	25.5 ± 0.3	16.96 ± 0.07	9.33 ± 0.06	7.29 ± 0.09
^{238}U (NuPulse)	29.4 ± 0.9	14.7 ± 0.4	11.4 ± 0.4	8.4 ± 0.6
^{232}Th (HPGe)	32.0 ± 0.4	17.48 ± 0.10	9.95 ± 0.10	7.10 ± 0.10
^{232}Th (NuPulse)	36.0 ± 0.3	14.20 ± 0.16	10.04 ± 0.15	8.1 ± 0.2

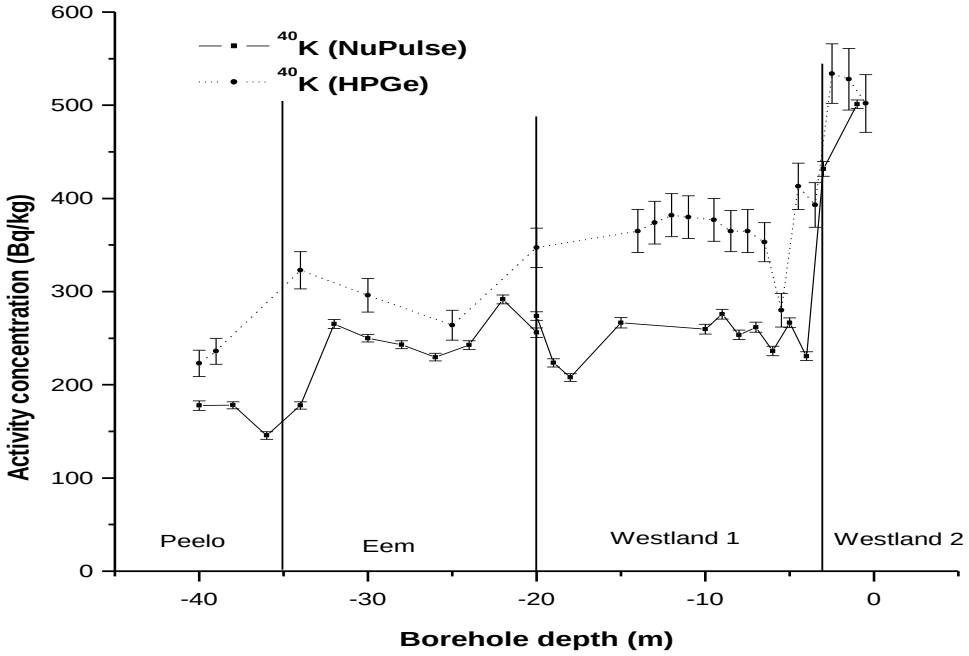

Figure 4.11: *Activity concentrations of ^{40}K for various formations in the KVI borehole as obtained by the NuPulse instrument and the KVI-HPGe detector system.*

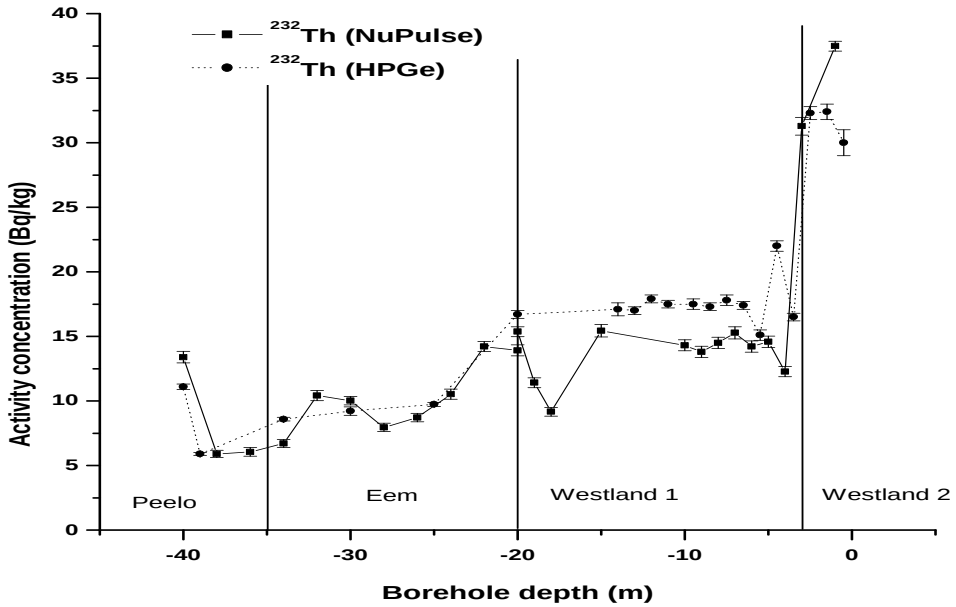

Figure 4.12: *Activity concentrations of ^{232}Th for various formations in the KVI borehole as obtained by the NuPulse instrument and the KVI-HPGe detector system.*

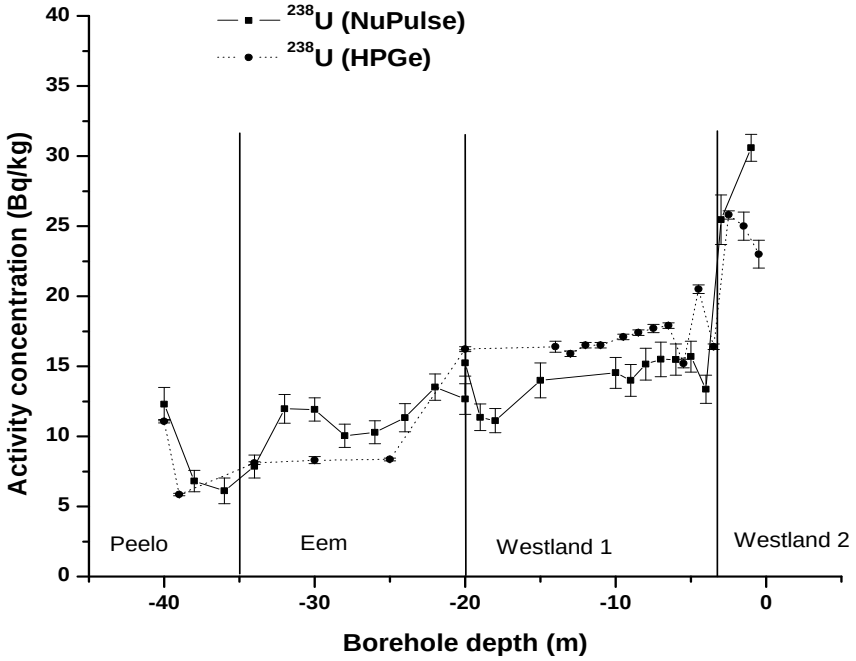

Figure 4.13: *Activity concentrations of ^{238}U for various formations in the KVI borehole as obtained by the NuPulse instrument and the KVI-HPGe detector system.*

4.3.2 Concrete tank and borehole experiments with PNDT-on configuration

As a follow-up to section 4.3.1, the neutron generator was incorporated into the NuPulse instrument to investigate neutron-induced gamma-ray production. As neutrons interact with formations, various reactions are possible, e.g. (n,γ), (n,n'γ), (see also section 4.1) whereby in principle the energies of the emitted gamma-rays will provide information on the emitting nuclei. Similar to the PNDT-off experiments, sets of test measurements were acquired for the PNDT-on settings.

4.3.2.1 Empty and water filled tank

The NuPulse instrument (with D-T neutron source connected) was first deployed inside an empty tank, followed by a deployment in a water-filled tank. For an empty tank, the bulk structure of the tank is thought to be mainly composed of concrete (SiO_2), iron (Fe) bars to support the walls, the surfaces beneath and walls adjacent to the tank (H_2O + SiO_2). For the water-filled tank, the concrete walls and the surface are shielded by a layer of water (about 1 m and >0.2m, respectively). The spectra for the empty and water-filled tank, shown in figure 4.14, show contributions from reactions of neutrons and the nuclei of the above mentioned materials and will be discussed below. The spikes in both spectra are due to an electronic digitizer and were considered not a serious concern to do a qualitative evaluation of the results. As a follow-up, we further verify the qualitative analysis of the spectra by comparison to a simulated spectrum.

Initially the BGO detector was calibrated using standard gamma-ray sources in the energy range of about E_γ = 0.2 - 2.7 MeV, see also section 4.2.1. As an approximation, we assumed the linear relation between channel number and energy up to E_γ = 9 MeV. The horizontal scale in figure 4.14 is therefore presented in an energy scale and not in channel numbers. In the water spectrum, we assumed that two reactions $^{1}H(n,\gamma)^{2}H$ and $^{16}O(n,n'\gamma)^{16}O$ will dominate with resulting gamma-ray energies of E_γ = 2.22 and 6.13 MeV, respectively. The reactions expected are controlled by their neutron cross sections, hence specified isotopes are stated. In the empty tank, mainly the $^{28}Si(n,n'\gamma)^{28}Si$ and $^{16}O(n,n'\gamma)^{16}O$ reactions were expected to dominate with resulting gamma-ray energies of E_γ = 1.78 and 6.13 MeV, respectively.

The effect of the $^{56}Fe(n,n'\gamma)^{56}Fe$ reaction still requires further checking as it could not be properly identified. In addition to the iron bars used to support the concrete structure of the tank, an iron 'stopper' (15 cm long, 6 cm diameter) is placed in front of the BGO detector to minimize direct neutron interaction with the BGO detector. One would expect, based on its proximity to the detector, that this stopper will be the main contributor to the gamma-ray spectrum due to interactions of neutrons with iron. In the empty tank spectrum as shown in figure 4.14, we show the full-energy peaks that we assumed to be associated with the Fe reactions. In the water-filled spectrum, no similar peaks are found.

Both spectra in figure 4.14 at higher energies are dominated by a continuum, and the $^{16}O(n,n'\gamma)^{16}O$ full energy peak at E_γ = 6.13 MeV is also spread over a broad range. The broad peaks include also both the single and double-escape peak contributions and are mainly associated with the poor energy resolution of the BGO

detector. One of the most remarkable features of the spectra in figure 4.14 is the fact that the intensity of the spectrum for an empty tank is a factor of 2 to 5 higher than the water-filled spectrum, despite the almost infinite mass of water (about 6.5 tons) in the latter condition. From the comparison it appears that the empty spectrum contains a component with energies of E_γ = 6 - 8 MeV, which is missing in the water filled spectrum.

To check this remarkable feature the intensities of the two spectra, with similar conditions for the water-filled and empty tank were simulated in MCNPX. In both cases, in addition to the properties of the concrete and the detector one has to include the soil on which the tank is placed and on one side of the tank the walls of the building in its near vicinity. The soil on which the tank is placed consists of a concrete platform with unknown thickness, placed on top of the soil. The walls consist in the lower part of about 50 cm concrete and higher up of bricks. In view of the absorption of gamma-rays and a first estimate of the importance of including these conditions in the modelling, simulations were carried out for the standard thickness of the concrete tank (10 cm) and for the situation, in which the thickness of the bottom plate is 120 cm and the wall of the tank is 60 cm. The description of the detector materials and the concrete is listed in Appendix C.

Figure 4.15(a) shows the *photon-flux* spectrum at the BGO detector for the water-filled tank, with and without contributions from the surrounding of the tank. As expected from the absorption of gamma-rays by water, there is hardly a difference noticeable in the spectra. This result is in contrast with the results in figure 4.15(b), where the intensity of the photon flux from an empty tank is a factor of 4 higher, if the surrounding is taken into account. The results of the simulations also indicate that the photon-flux has a considerable component in the region E_γ = 6 - 8 MeV. The conclusion drawn from these simulations is that for an empty tank, the induced gamma-radiation in the surrounding soil and walls is a dominant component in the gamma-ray spectrum. In retrospect this is not surprising in view of the extension of the soil and the walls and their associated masses.

In the next steps the response of the BGO detector is included in the MCNPX simulation. The results are presented in figure 4.16 in comparison with the data: in the top part for the water-filled tank and on the bottom part for an empty tank. The comparison is based on the calibration factor of $\varepsilon = 0.537 \pm 0.015$, as obtained from the PNDT-off measurements (section 4.3.1). From the comparison it becomes clear that the simulated results reveal more structure than the ones observed, but the two main peaks are quite well reproduced. The influence of the surroundings in the water-filled tank spectrum is hardly noticeable, as expected from the photon-flux spectrum in figure 4.15a. For the empty tank, the washed-out structure in the measured spectra is likely related to the occurrence of processes not included in the simulations. The two main missing processes in the simulation are likely coincidence summing in the BGO detector and shortcomings in the cross-section data. The first is likely due to the large effective volume and solid angle of the detector and the high count rate in the detector.

The MCNPX code available at the RuG/KVI employs the ACTI cross-section data, processed from the ENDF/B-VI library, where the neutron-capture cross section and corresponding secondary photon distributions were updated for ^{16}O (Frankle *et al.*, 2002). These data libraries are also supposed to account for the possible reactions ^{16}O(n,x γ) for neutron energies of E_n = 14 MeV. Moreover, another cross-section data library, the Oil-Well Logging (OWL) evaluation (Hogenbirk, 2004) was applied, but there were no major differences to the simulated spectrum in figure 4.16a. The photon

angular distribution in the present model will have less effect since the BGO detector has a large effective volume for gamma-radiation.

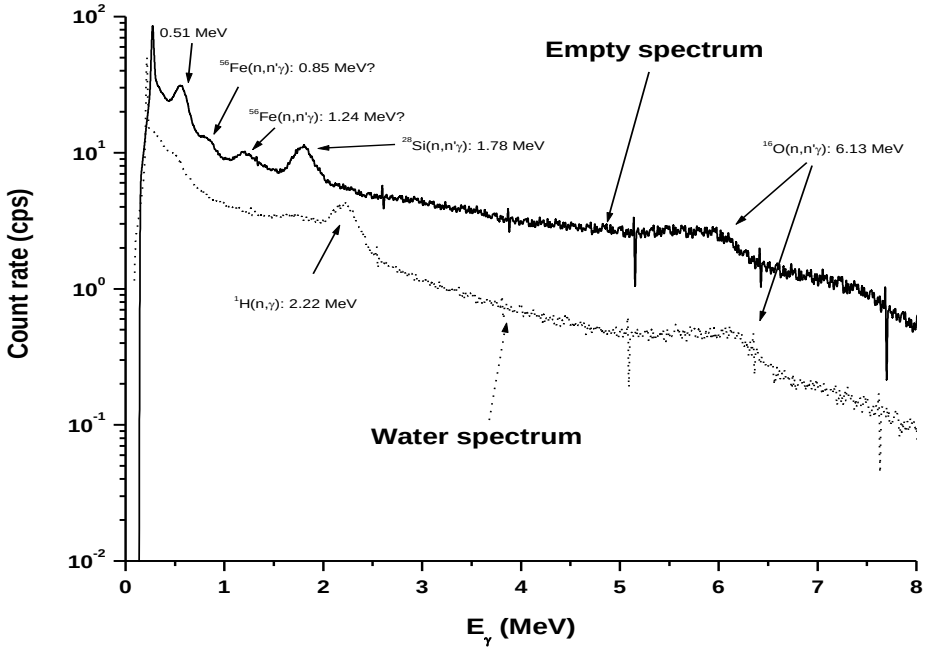

Figure 4.14: *Gamma-ray spectra measured in an empty and a water filled tank for the PNDT-on settings. The peaks are labelled with their energy and the reaction from which they originate. For the $^{56}Fe(n,n'\gamma)$, reaction and energies shown are not certain, hence the ? sign. The negative spikes in the spectrum are an artefact due to a shortcoming in the electronic digitizer.*

For the situations of the NuPulse instrument operations, the possible $^{16}O(n,x\,\gamma)$ reactions are presented in column 1 of table 4.6. Included also in table 4.6 are the minimum neutron energies required to open the specified reaction channel. From table 4.6, one may conclude that the $^{16}O(n,\alpha\,\gamma)^{16}O$ reaction should be observed in the simulated spectrum in figure 4.15. Further tests on the validity of the incorporated cross-section data libraries are investigated to allow the intended quantitative analysis of the PNDT-on spectra.

Table 4.6: *Neutron threshold energies for various ^{16}O reactions including the dominant secondary gamma-rays produced.*

Reaction	Neutron threshold energy	Dominant gamma-rays (MeV)	Reference
$^{16}O(n,n'\gamma)\,^{16}O$	7 MeV	6.13, 6.92, 7.12	Knoll, 2000
$^{16}O(n,p\gamma)\,^{16}N$	10 MeV	6.13, 6.92, 7.12	Knoll, 2000; Subaşi, 2000
$^{16}O(n,\alpha\gamma)\,^{13}C$	3 MeV	3.68, 3.85	Hale, 2001
$^{16}O(n,n'\alpha\gamma)\,^{12}C$	12 MeV	4.44	Nelson, 2001

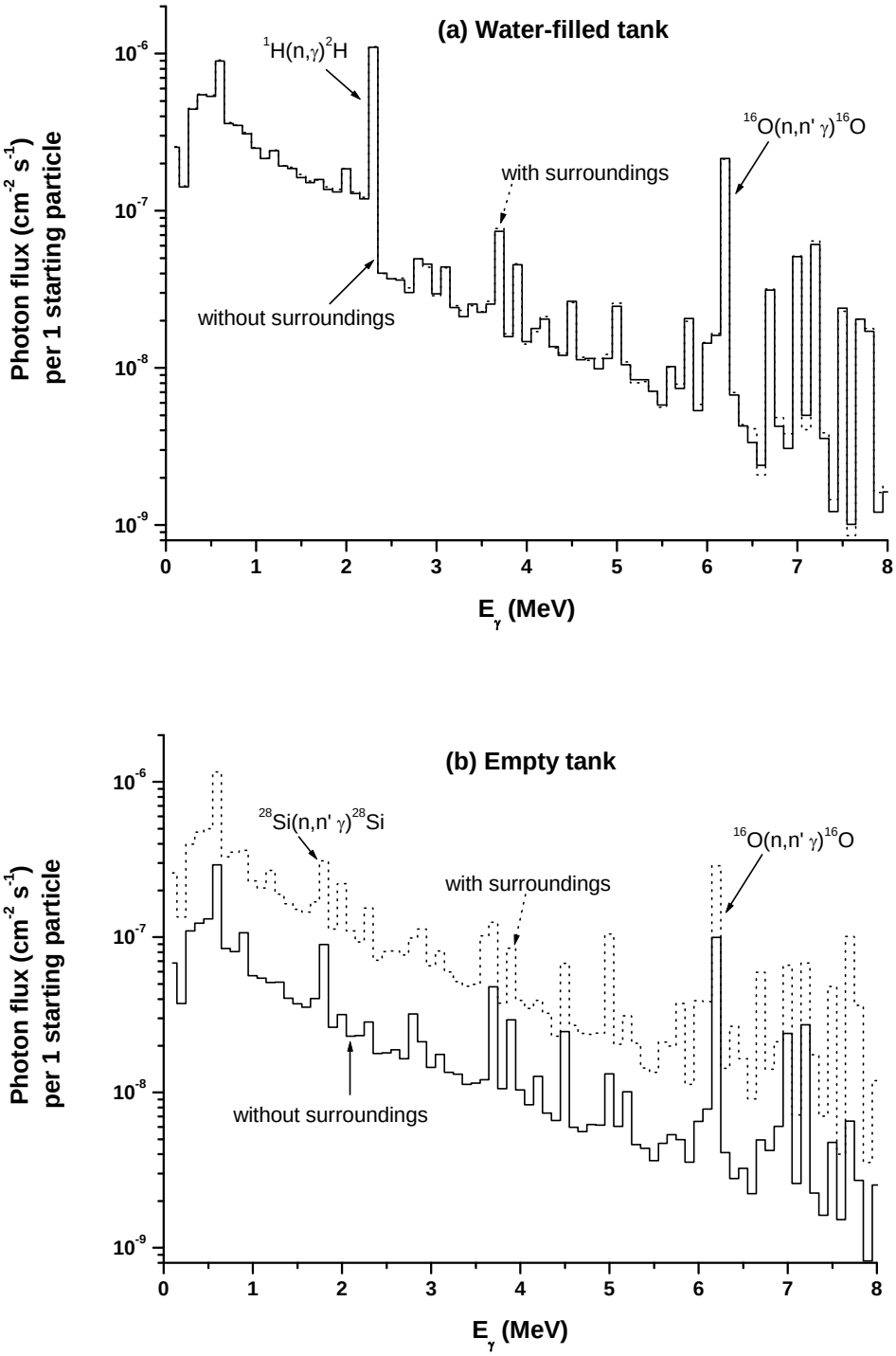

Figure 4.15: *MCNPX photon flux for the (a) water-filled and (b) empty tank showing the dominant full-energy peaks with the originating reactions.*

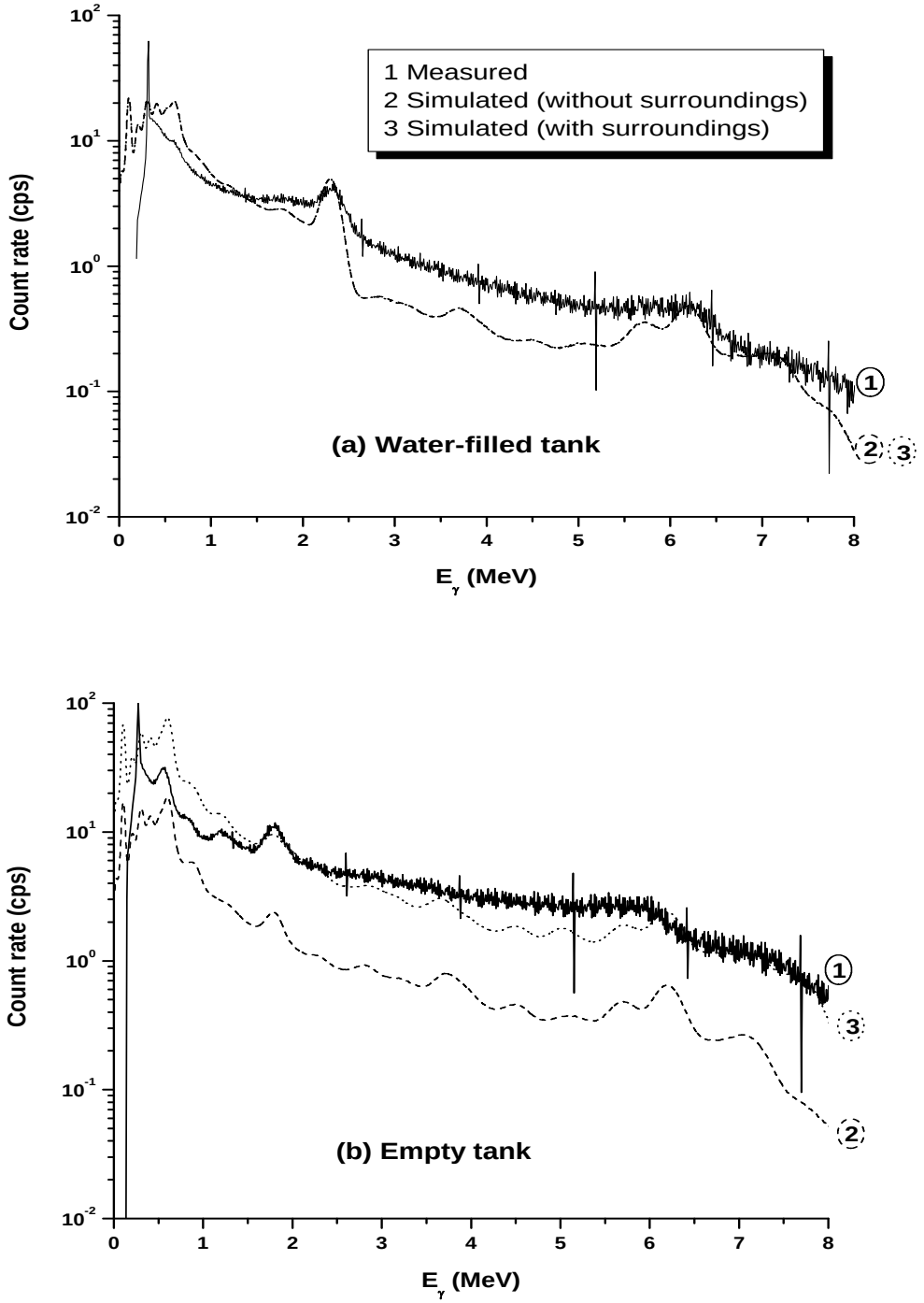

Figure 4.16: *Measured and MCNPX-simulated gamma-ray spectra for (a) a water filled tank and (b) an empty tank. Note that the vertical scale is presented on a logarithmic scale.*

In the beginning of 2009 we came to the conclusion that all possibilities trying to describe the empty tank and water-filled tank spectra with MCNPX were exhausted and it was decided to investigate the spectra with another Monte Carlo code, FLUKA (FLUktuierende KAskade) (Ferrari *et al.*, 2005) to find out if the discrepancies were code related. In view of the several extra years that were spent to investigate the possible causes for the discrepancies between the results of MCNPX simulations and measurements with the tank, only the spectra for the tank related experiments were investigated (empty tank, water-filled tank and KCl dissolved in water).

For the simulation of this test we used FLUKA 2008 version 3b. Similar to MCNPX (see 3.8.4), FLUKA is a general-purpose code for simulating the interaction of radiation with matter, covering an extended range of applications, from high-energy physics to medical and radiation physics (Ferrari *et al.*, 2005). In FLUKA, neutrons with energies below E_n = 20 MeV are classified as low-energy neutrons and their transport uses a multi-group energy approach (see description in intermezzo 3.2). In this approach, the neutron energy ranges are divided into a given number of discrete energy groups, i.e. 260 groups with the upper energy limit of E_n = 20 MeV and the low-energy limit of 10^{-5} eV (Ferrari *et al.*, 2005). Thus, elastic and inelastic reactions are simulated not as individual processes but by group-to-group transfer probabilities forming the down-scattering matrix (Ferrari *et al.*, 2005). The down-scattering matrix provides the probability for a given neutron energy group to generate a photon in each of 42 gamma-ray energy groups, with an energy of 1 keV ≤ E_γ ≤ 50 MeV. The matrix includes capture gamma-rays as well as gamma-rays produced in other inelastic reactions.

The photon energy is sampled randomly in the energy interval corresponding to its gamma-ray group, see table 4.7 for the selected gamma-ray energy groups. Moreover, in table 4.7, the width of some energy intervals between two adjacent groups is about 500 keV, a rather large interval that may have positive/negative effects on the results. This energy-interval feature differs from the continuous approach available to MCNPX based cross-sections (see also section 3.8.4). More information and capabilities of FLUKA can be found in the code manual (Ferrari *et al.*, 2005) and also on the website (http://www.fluka.org/fluka.php).

FLUKA bases the calculations on recent evaluation data libraries, e.g., ENDF/B-VIR8, JEFF-3.0 and JENDL-3.3. For most of the materials in FLUKA the cross-section libraries are comparable to the recent available data libraries used in MCNPX, for example for ENDF/B-VI.8 only the implementation approach differs.

As an initial test, simulations with a modified NuPulse instrument setting were calculated using FLUKA and MCNPX codes. The geometry settings for both codes are explained in more details in intermezzo 4.2. In the first test, the water-filled tank was modelled in both codes and subsequently the empty tank. Note also, that for the empty tank, the walls of the concrete were made thicker to include the building walls next to the tank and soil beneath the tank.

The results presented in figure 4.17 show differences in fluxes depending on which code was used. Most strikingly is the difference in magnitude of the continuum for E_γ > 1 MeV, where the spectra calculated by FLUKA, are more flat than those calculated by MCNPX, causing an intensity difference of an order of magnitude at E_γ ~ 6 MeV. Another striking difference is the width of the peaks, which is related to the group structure of the energy interval in FLUKA. As pointed out, the broadening in the FLUKA spectra is caused by the random sampling of the energy within its interval (see also table 4.7). In more detail: the resulting secondary gamma-rays produced by continuous cross-section data libraries implemented in MCNPX, show distinct

dominant full-energy peaks compared to the multi-group approach of FLUKA. The FLUKA results show the structures that are resembling the experimental spectra in figure 4.14: above the dominating continuum structure we find distinct peaks at E_γ = 2.22 MeV corresponding to the $^{1}H(n,\gamma)^{2}H$ reaction[5] and a broad peak in the E_γ = 6 - 7 MeV region due to $^{16}O(n,n'\gamma)^{16}O$ reactions. In the E_γ = 3 - 4 MeV region of FLUKA calculations, the broad peak is also present but not as clearly resolved as in MCNPX spectra. In the E_γ = 6 - 7 MeV energy region of MCNPX spectra, the distinct peaks as predicted from table 4.6 are clearly noticeable. Moreover the E_γ = 6.92 and 7.12 MeV peaks are missing in FLUKA calculations are incorporated in the broad peak in the 6-7 MeV region. As pointed out, this is one of the differences in the treatment of gamma-ray energies in the two codes. Additionally, MCNPX results reveal the $^{28}Si(n,n'\gamma)^{28}Si$ reaction with a gamma-ray energy of E_γ = 1.78 MeV in the empty tank spectrum. In contrast in FLUKA calculation, this energy will be sampled randomly within an energy interval of $\Delta E_\gamma \sim 340$ keV, hence a flat structure is observed.

Furthermore, in figure 4.18, we show simulated spectra using MCNPX and FLUKA for the transport of a gamma-ray event with E_γ = 1.46 MeV, similar to PNDT-off settings. The full-energy peak is well reproduced in both codes. FLUKA shows the single escape peak somewhat shifted to higher energy which is related to the energy grouping as presented in table 4.7. Moreover, the intensities in the continuum region are higher in FLUKA for $E_\gamma > 0.6$ MeV, which cannot be explained by the energy binning and hence point to other differences between the MCNPX and FLUKA codes. We also note that the difference in magnitude of a factor of four between FLUKA and MCNPX in the PNDT-on simulations does not show up in this PNDT-off simulation. This may hint to differences in the transport of neutrons.

Table 4.7: *Selected gamma-ray energy intervals implemented in FLUKA calculations for gamma-ray energies of 100 keV up to 12 MeV. For each energy-group the lower limit and the upper limit and also the width of each group are presented.*

Energy-group (MeV)	Width	Energy-group (MeV)	Width
10 - 12	2000 keV	2.0 – 2.5	500 keV
8 - 10	2000 keV	1.66 – 2.0	340 keV
7.5 – 8	500 keV	1.5 – 1.66	160 keV
7.0 – 7.5	500 keV	1.34 – 1.5	160 keV
6.5 – 7.0	500 keV	1.33 – 1.34	10 keV
6.0 – 6.5	500 keV	1.0 – 1.33	330 keV
5.5 – 6.0	500 keV	0.8 – 1.0	200 keV
5.0 – 5.5	500 keV	0.7 – 0.8	100 keV
4.5 – 5.0	500 keV	0.6 – 0.7	100 keV
4.0 – 4.5	500 keV	0.45 – 0.6	150 keV
3.5 – 4.0	500 keV	0.3 – 0.45	150 keV
3.0 – 3.5	500 keV	0.2 – 0.3	100 keV
2.5 – 3.0	500 keV	0.1 – 0.2	100 keV

[5] Gamma generation in FLUKA is treated in the multi-group scheme with the exception of the E_γ = 2.22 MeV transition of Deuterium where the actual photon energy is provided and not randomly sampled within the energy interval (Ferrari, 2005).

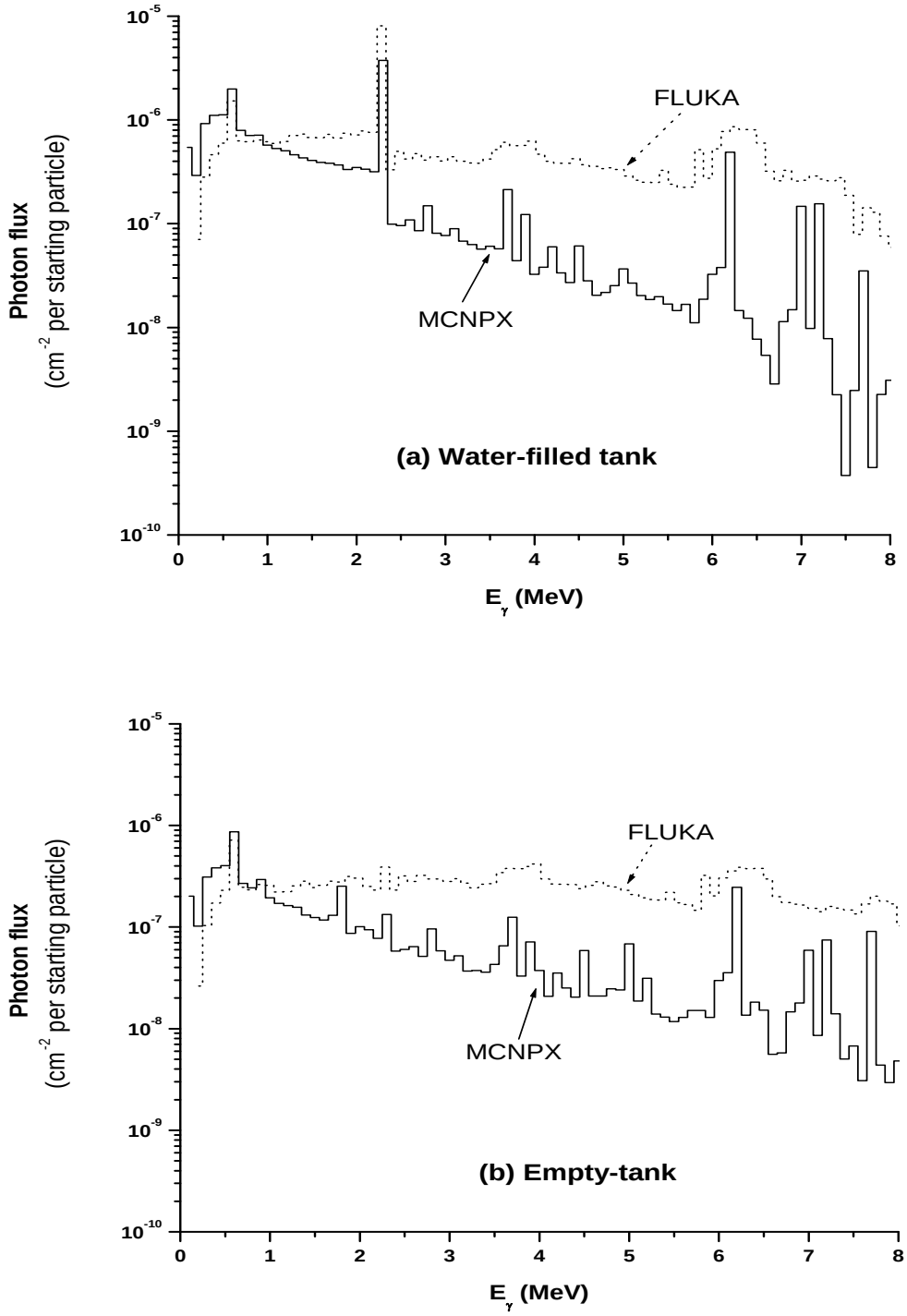

Figure 4.17: *Photon flux for the water-filled and empty tank using the two Monte Carlo codes, MCNPX and FLUKA.*

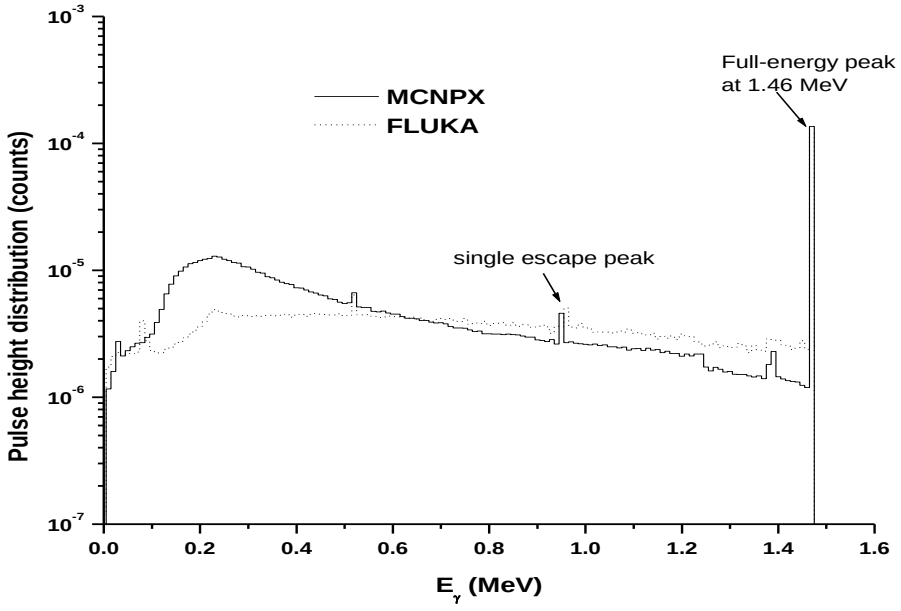

Figure 4.18: *Unbroadened pulse height spectrum for the gamma-rays from ^{40}K decay simulated by MCNPX and FLUKA codes showing the energy deposition in the BGO detector.*

Intermezzo 4.2: MCNPX and FLUKA simulation approaches

For the purpose of the simulation, a concrete tank filled with water was assumed as shown in figure 2. For both MC codes, inside the tank in addition to water, the gamma-ray detector system (BGO covered only with Cd layer) was modelled and shielded from an isotropic point neutron source (energy 14.2 MeV) with a neutron stopper (modelled as stainless steel). The geometry as modelled is a simplified NuPulse tool. In the initial comparison, only major components were considered. In the follow-up tests, an empty tank was considered with much more thicker walls and the soil surface beneath the tank was included.

In the input stream of FLUKA, geometries are defined using bodies (similar to what is referred to as surfaces in MCNPX) and regions (cells in MCNPX). RCC represents the usual right circular cylinder as used also in MCNPX macrobodies settings. The bottom line represents the region (cells) that will be bound by the given bodies.

```
*          1         2         3         4         5         6         7         8
RCC body7          0.0       0.0      +1.2       0.0       0.0     +18.0
                   2.5
*
regbg7    5    +body5    -body6    +body7
```

Figure 1: *An example of FLUKA geometry input card.*

In the input stream of MCNPX, the cell card includes the material number, which we define later. In a similar fashion with FLUKA, one has to define all the materials required, and then assign each material to a specific region. The detector is therefore included as another region with the correct material composition. In both cases, we used the isotropic point source inside the tank and both codes require the starting energy of a particle, its direction (in this test isotropic), particle type and initial position.

In FLUKA one can define a single-element material or a compound. FLUKA has pre-defined material names that one can refer to by material (element) number 1 – 25. For other elements not in the list, a new material can be defined and assigned with a material number not in the list, i.e. any number from 26 upwards. Together with the material specifications, in other instances the LOW-MAT card is required for low-energy neutron transport (any neutron with $E_n \leq 20$ MeV).

In this example, the cross-section data libraries used in FLUKA modelling are mainly from; ENDF/B-VIIR0 (H), ENDF/B-VIR8 (O, Bi); ENDF/B-VII (Ge) and JENDL-3.3 (Cd). All the FLUKA cross sections used are processed at a temperature of 296 K. For most of the materials, the cross section libraries are comparable to the ones in MCNPX, e.g. ENDF/B-VI.8.

In these comparisons, no variance reduction methods were implemented. In FLUKA, USRTRACK, the track-length fluence estimator was used to score the differential distribution of gamma-rays in the BGO region. For MCNPX, we used the flux F4 tally in the BGO detector. Also to be consistent, 100 keV energy bins (for gamma-rays) were used in both codes, with 100 keV the lower limit and 8 MeV the highest energy. To speed-up the calculations, the following energy cut-offs were incorporated: for electrons, positrons and photons 100 keV and for neutrons 10^{-5} eV.

In addition, for the FLUKA input we used the default settings 'NEW-DEFAults'. With this default setting, some of the relevant physical effects considered are:

- EMF on - activates ElectroMagnetic FLUKA; transport of electrons, positrons and photons
- Inelastic form factor corrections to Compton scattering activated
- Low-energy neutron transport down to thermal energies included. The neutron high-energy threshold is set at $E_n = 20$ MeV.
- Non-analogue absorption for low-energy neutrons with probability p=0.95 for the last (thermal) groups.
- Heavy particle e^+e^- pair production activated with full explicit production (with the minimum threshold = $2\ m_e c^2$)

Figure 2: *Geometrical set-up for the water-filled tank as modelled in the MCNPX and FLUKA simulations. The dimensions are drawn not to scale.*

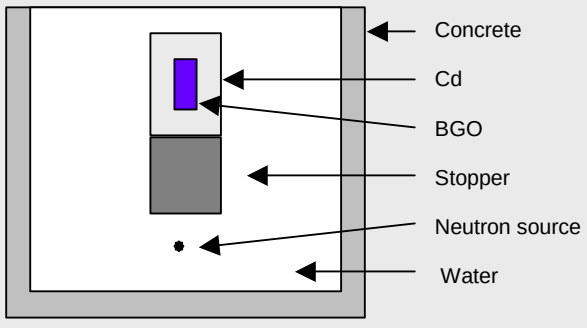

In experimental results presented in figure 4.14, the $^{28}Si(n,n'\gamma)^{28}Si$ reaction is clearly observed, but due to the effect of the broad energy-binning intervals used in FLUKA simulations, this gamma-ray energy is hardly noticeable in the FLUKA spectrum. In FLUKA, the calculations use cross-section data on natural silicon and MCNPX simulates silicon as separate isotopes (^{28}Si, ^{29}Si and ^{30}Si). To investigate the consequence of such differences, an earlier version of the data library, ENDF/B-VI.0 (evaluation year, 1976) available in MCNPX, was used to replace the isotopic silicon by natural silicon. The results as presented in figure 4.19 show consistency in MCNPX data libraries. As evident from figure 4.19, for the same element, FLUKA and MCNPX show largely different results in intensity. We also note that, both the FLUKA and MCNPX codes use similar data libraries for the recent silicon cross section. Furthermore, the multi-group neutron data available in MCNPX produced in 1987 (Little, 1987; Pelowitz, 2005) could not improve the results relative to the FLUKA results. In FLUKA, the neutron multi-group approach uses 260 groups compared to 30 groups in MCNPX, and 42 groups for gamma-rays in FLUKA compared to 12 groups in MCNPX. The gamma-ray 12-groups structure available in MCNPX has intervals[6] of about 1 MeV for the energies of interest to this study (Little, 1987).

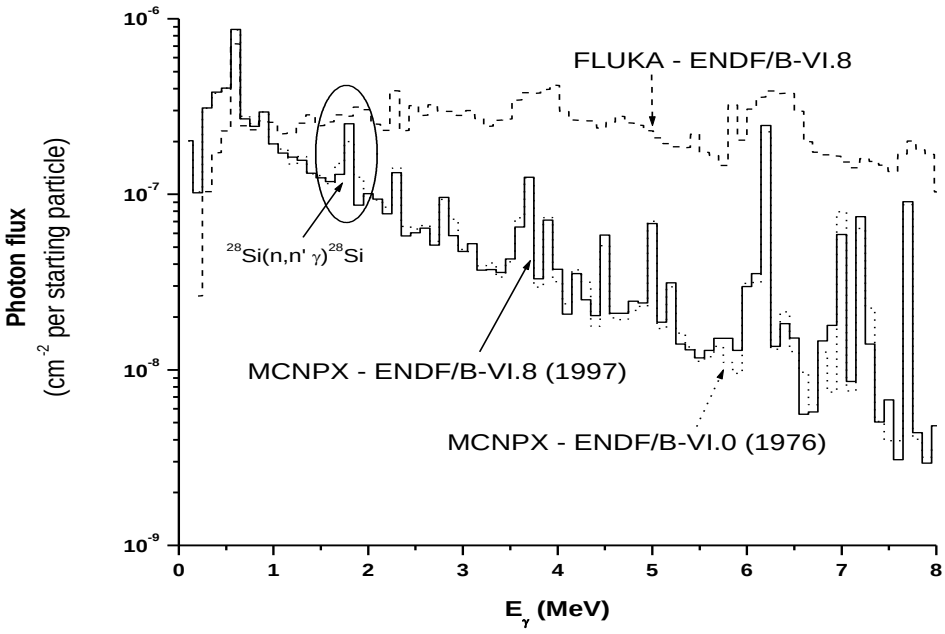

Figure 4.19: *Photon flux for an empty tank using the MCNPX and FLUKA codes; the cross section data libraries used for assessing the reaction on silicon are indicated.*

Next, the reaction cross sections on oxygen for both codes were investigated. In this test, an imaginary detector made of pure hydrogen with density 100 g cm^{-3} was used with a surrounding environment entirely consisting of oxygen (ρ = 1.141 g cm^{-3}).

[6] The gamma-ray energy group intervals available for the MCNPX multi-group approach: E_γ = 20-9 MeV, 8-9 MeV, 7-8 MeV, 6-7 MeV, 5-6 MeV, 4-5 MeV, 3-4 MeV, 2-3 MeV, 1-2 MeV, 0.5-1 MeV and 0.1-0.5 MeV (Little, 1987).

Both FLUKA and MCNPX deploy the ENDF/B-VI.8 data libraries for oxygen reactions. The results are presented in figure 4.20 and clearly indicate the reactions on ^{16}O are as expected from table 4.6 in both codes. The peaks appear differently due to the broadening implemented in FLUKA. In addition to the continuous approach implemented in MCNPX, one can also request to apply the discrete data tables for the cross sections. The results further emphasise consistency within a factor of two in cross sections for both approaches in MCNPX, but highlight that a clear difference in magnitudes remains with the FLUKA multi-group approach.

Further de-convolutions of the MCNPX simulated water spectrum presented in figure 4.16 were investigated. Figure 4.21 shows the simulated water spectrum and simulations of each component separately. The reactions are based on components that we assumed would be prominent in the resulting reactions. The components are divided as follows: BGO representing the neutron interaction with the BGO crystal, $^{1}H(n,\gamma)^{2}H$ and $^{16}O(n,n'\gamma)^{16}O$ reactions with water and all other components that make up the complete instrument. Unfortunately, a comparison with FLUKA was not possible due to limitations in the FLUKA code. In MCNPX, one can flag the contribution of a chosen material and request only its contribution to the detector material. Representation of these components relies mainly on information that could not be properly verified, e.g. the full material composition of the stopper.

Another important aspect to consider is that high fluxes of thermal neutrons increase the competition of materials for all other possible reactions. As explained above, due to the flexibility of simulations with MCNPX, it is possible to separate contributions for each relevant component. One difficulty, that immediately emerges, is the presence of oxygen in both the gamma-ray detector (BGO) and the water in the tank. The main reaction of neutrons with oxygen occurs with fast neutrons. The BGO detects direct flux passing through the iron stopper and this flux may even be considerably higher than the scattered flux of partly moderated neutrons in water. To verify the effect of the relative contribution of oxygen present in the BGO crystal, the detector was replaced with an imaginary Pb-crystal. The results as presented in figure 4.22 reveal that the contributions due to oxygen from BGO is relatively small compared to secondary gamma-rays from the water sample.

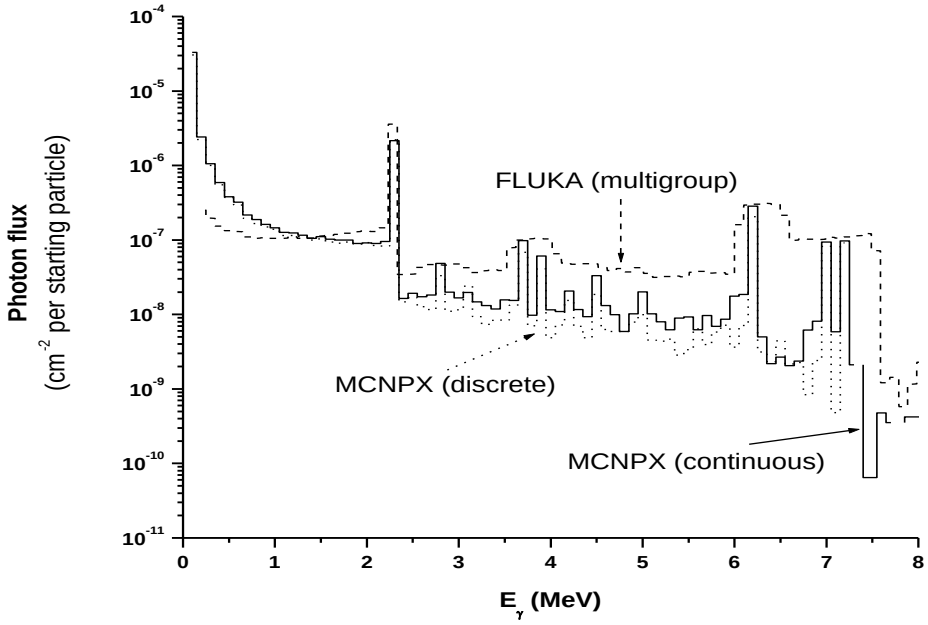

Figure 4.20: *Photon flux estimates using MCNPX and FLUKA to investigate the cross section data implementation for $^{16}O(n,x\,\gamma)$ reaction.*

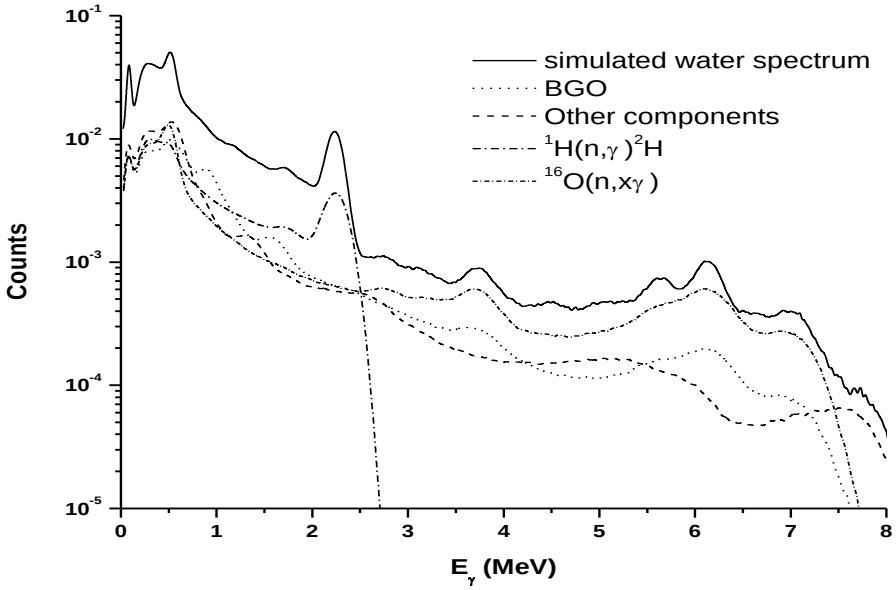

Figure 4.21: *The MCNPX simulated water spectrum is presented including the spectra of the major components that contribute to the final spectrum.*

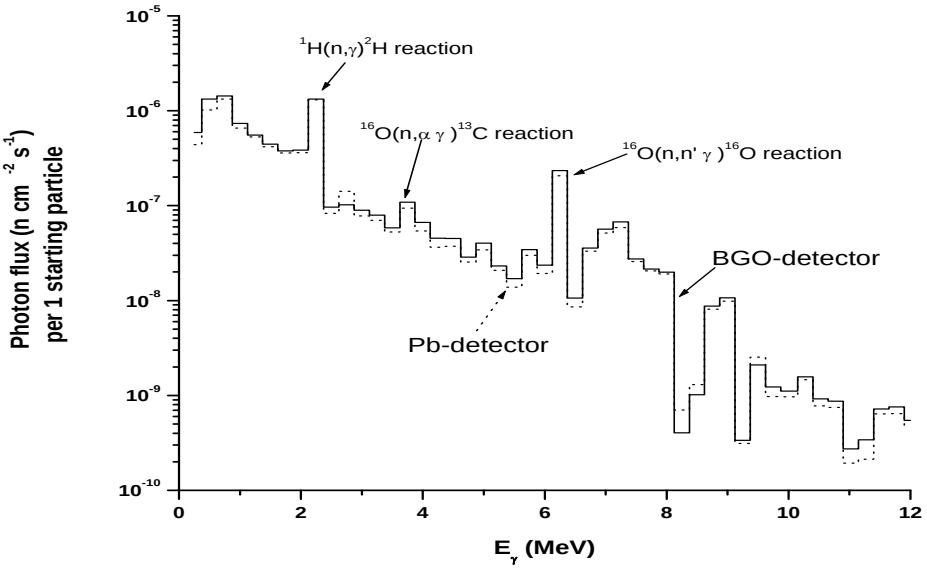

Figure 4.22: *Estimated photon flux in the simulated NuPulse instrument with the BGO-crystal replaced by a Pb-crystal for comparison.*

We note that the water-filled tank represents the simplest geometry and it is imperative for further investigations of known/unknown samples, that this geometry is well described in the simulations. In figure 4.23, the measured spectra are presented together with the simulated spectra from both the MCNPX and FLUKA codes. Figure 4.23 (a) shows measured spectrum in the water-filled tank compared to the simulated spectra of similar conditions.

From the comparison it is to be concluded that neither of the two codes is able to reproduce the experimental data. FLUKA, partly because of its gamma-ray binning seems to reproduce the shape better but for $E_\gamma > 3$ MeV it overestimates the count rate by a factor of two. MCNPX simulations show more structure in the spectra than is observed and underestimate the count rate by a factor of two for $E_\gamma > 3$ MeV. Under those circumstances it is hardly justified to analyse more complex materials. In the following, we therefore remain confined to a particular phenomenon in water + KCl solutions and briefly present spectra obtained in the KVI borehole.

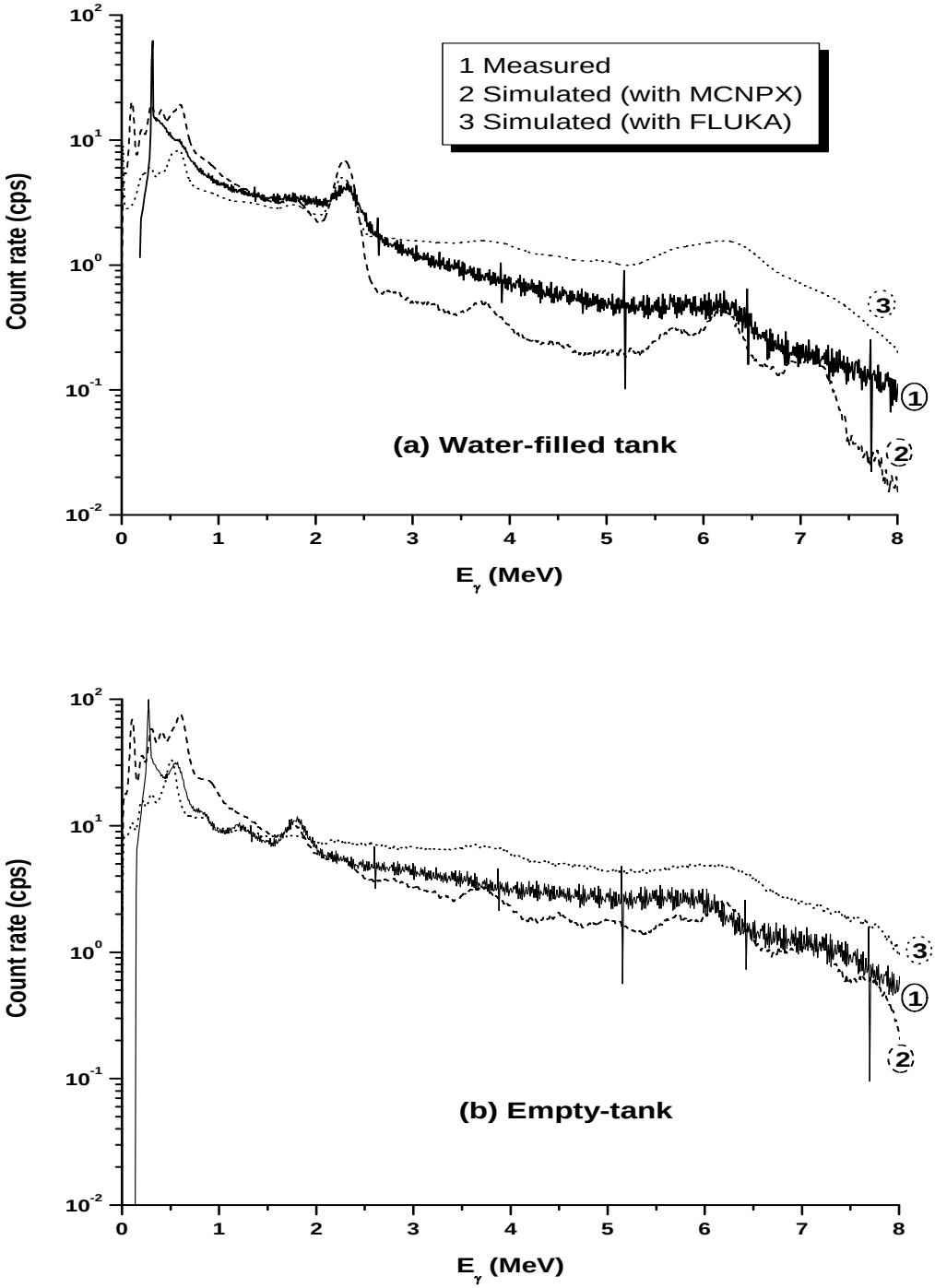

Figure 4.23: *Measured and simulated (with MCNPX and FLUKA) gamma-ray spectra for (a) a water-filled tank and (b) an empty tank.*

4.3.2.2 The solutions analysis of water+KCl

As indicated in section 4.3.1, also PNDT-on spectra were measured for the water+KCl-solutions. For each load of KCl added, similar to figure 4.6, PNDT-on spectra were acquired. The gamma-ray spectra for KCl-water mixtures are presented in figure 4.24. The analysis will focus mainly on a qualitative evaluation of the results. Thereafter, another attempt with simulation (both codes) analyses will be tested.

The measured spectra in figure 4.24 show that with increasing KCl content, the intensity of the E_γ = 2.22 MeV peak decreases due to the $^{1}H(n,\gamma)^{2}H$ reaction, but the intensity of the peak near E_γ = 6.12 MeV increases. Moreover, the natural potassium (^{40}K) line at E_γ = 1.46 MeV increases in strength as observed and explained in the PNDT-off spectra (see section 4.3.1). Especially chlorine (^{35}Cl) and to a lesser extend potassium (^{39}K) are relatively strong neutron absorbers (for thermal neutrons: $\sigma(^{35}Cl)$= 43.6 b and $\sigma(^{39}K)$ = 2.12 b compared to $\sigma(^{1}H)$= 0.33 b (Firestone, 1996)) via the $^{35}Cl(n,\gamma)^{36}Cl$ reaction and gamma-rays are expected at E_γ = 6.11, 6.22, 7.41 and 7.79 MeV. With the present BGO detector, these lines may not all be observed as individual lines. The count rates for $^{16}O(n,n'\gamma)^{16}O$ reactions depend on the fast neutron fluxes and in our experiments the addition of KCl has little effect on the fast neutron fluxes. As more KCl is dissolved in water, the intensity of the H peak decreases due to the competition for the absorption of thermal neutrons between ^{1}H, ^{39}K and ^{35}Cl (see intermezzo 4.3). Therefore, as more KCl is added, the characteristic peaks due to neutron capture by ^{35}Cl should become stronger and the E_γ = 2.22 MeV gamma-ray due to capture by ^{1}H should decrease in intensity. The intensities at high energies (E_γ > 5 MeV) increase indeed with the addition of KCl, in agreement with this expectation. It should be noted that the $^{35}Cl(n,\gamma)$ reaction which has a resulting gamma-ray with E_γ = 6.11 MeV energy, directly interferes with the 6.13 MeV gamma-ray energy from $^{16}O(n,n'\gamma)^{16}O$ reactions.

Figure 4.25 presents the relative ratios of the peak content at E_γ = 2.22 MeV and 6.11+6.13 MeV (both ^{35}Cl and ^{16}O full energy peaks) for the top and bottom panel, respectively. The ratios are calculated relative to the water spectra. As more KCl is added, the intensities of the E_γ = 2.22 MeV gamma-ray decrease by a factor of up to four in the measured spectra. In the simulated spectra, the intensities decrease only by a factor of up to two in both MCNPX and FLUKA. The results of the two simulations agree well with each other and the reduction to 50% at 275 kg of added KCl is well understood from the first-order estimate (see intermezzo 4.3). In this first-order estimate only thermal neutrons were considered. Mainly Cl (Sayer *et al.*, 2006) and to much lesser extent K (Mii *et al.*, 1987) have resonances in the energy range E_n > 1 eV. These resonances will remove fast neutrons and hence reduce the flux of thermal neutrons, leading to a faster than expected decrease of the E_γ = 2.22 MeV gamma-ray intensity.

In the bottom panel of figure 4.25, the intensities of the E_γ = 6.1 MeV peak increase by a factor of about 2 in the measured spectra and the simulated spectra are almost constant. Moreover in the measured spectra, for KCl mass ≥ 200kg, the pattern changes from an increasing to a decreasing peak-content. This pattern change is not replicated in the simulations data. This result can again be understood in terms of resonances, not all leading to gamma-ray emission. The fact that MCNPX and FLUKA simulations do not reproduce the trend in the data suggests that their treatment of neutron resonances is not adequate.

Furthermore, in figure 4.26, the measured spectra were directly compared to the simulated spectra from FLUKA and MCNPX. FLUKA simulated spectra for both masses represented in figure 4.26 show a good agreement with the measured spectrum. Once again, MCNPX results show more peak structures as compared to both the measured and FLUKA simulated spectra but the count rates are a factor of four too low for $E_\gamma > 2.5$ MeV. For $E_\gamma < 2$ MeV neither of the simulations reproduces the contribution to the spectrum from the natural decay of ^{40}K. In view of this missing component, the fact that the FLUKA simulations underestimate the count rate is less worrisome than the overestimate by MCNPX.

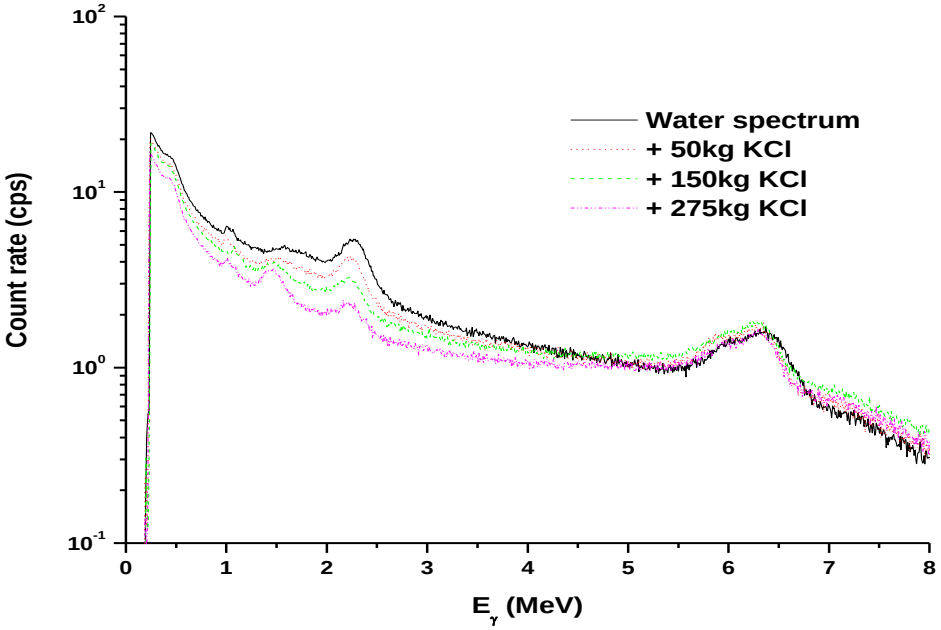

Figure 4.24: *Neutron-induced gamma-ray spectra for water with various masses of the dissolved KCl.*

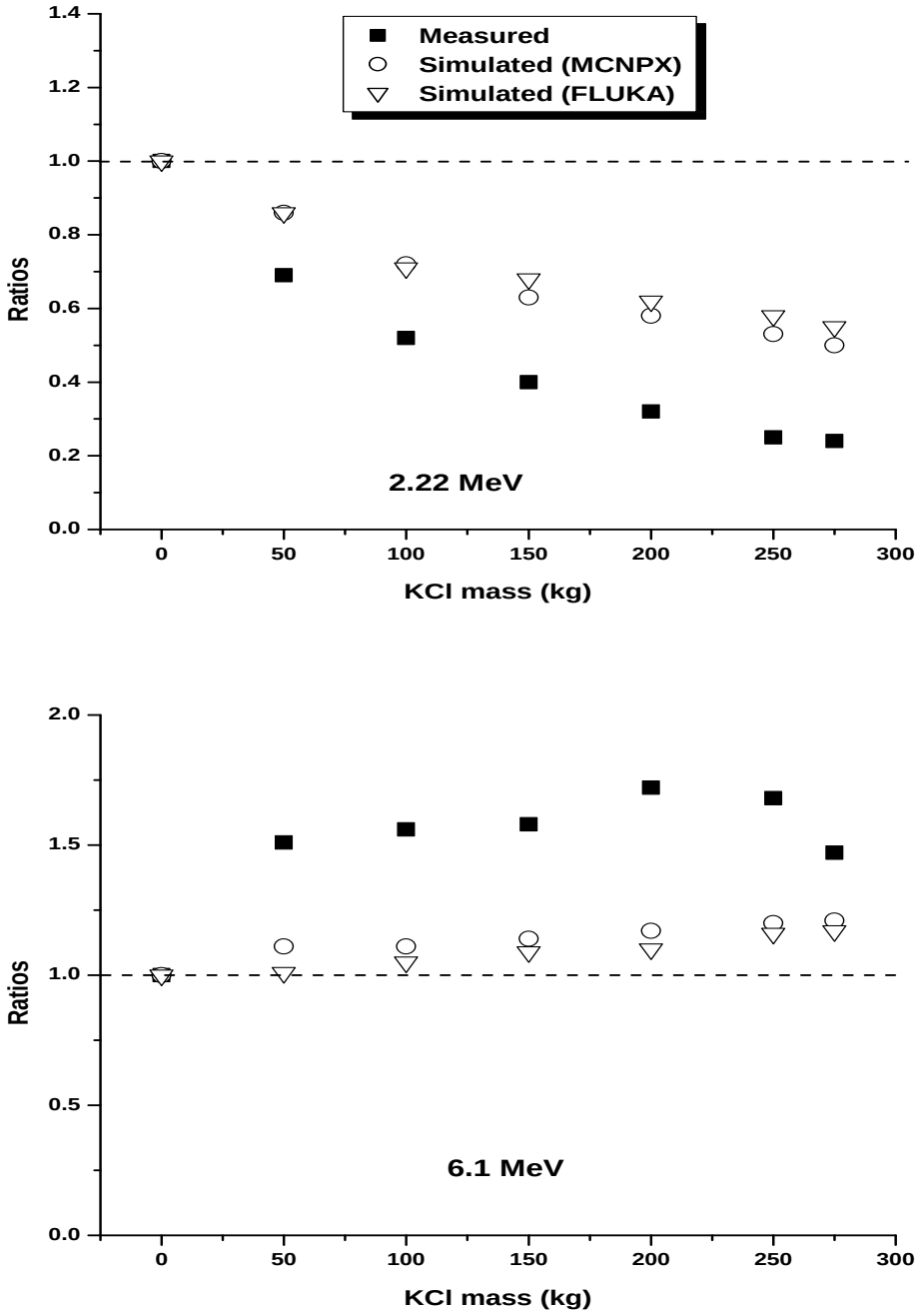

Figure 4.25: *Relative peak content ratios for the two full-energy peak regions in figure 4.24. The ratios are related to the peak content of the water spectra (0kg KCl mass added).*

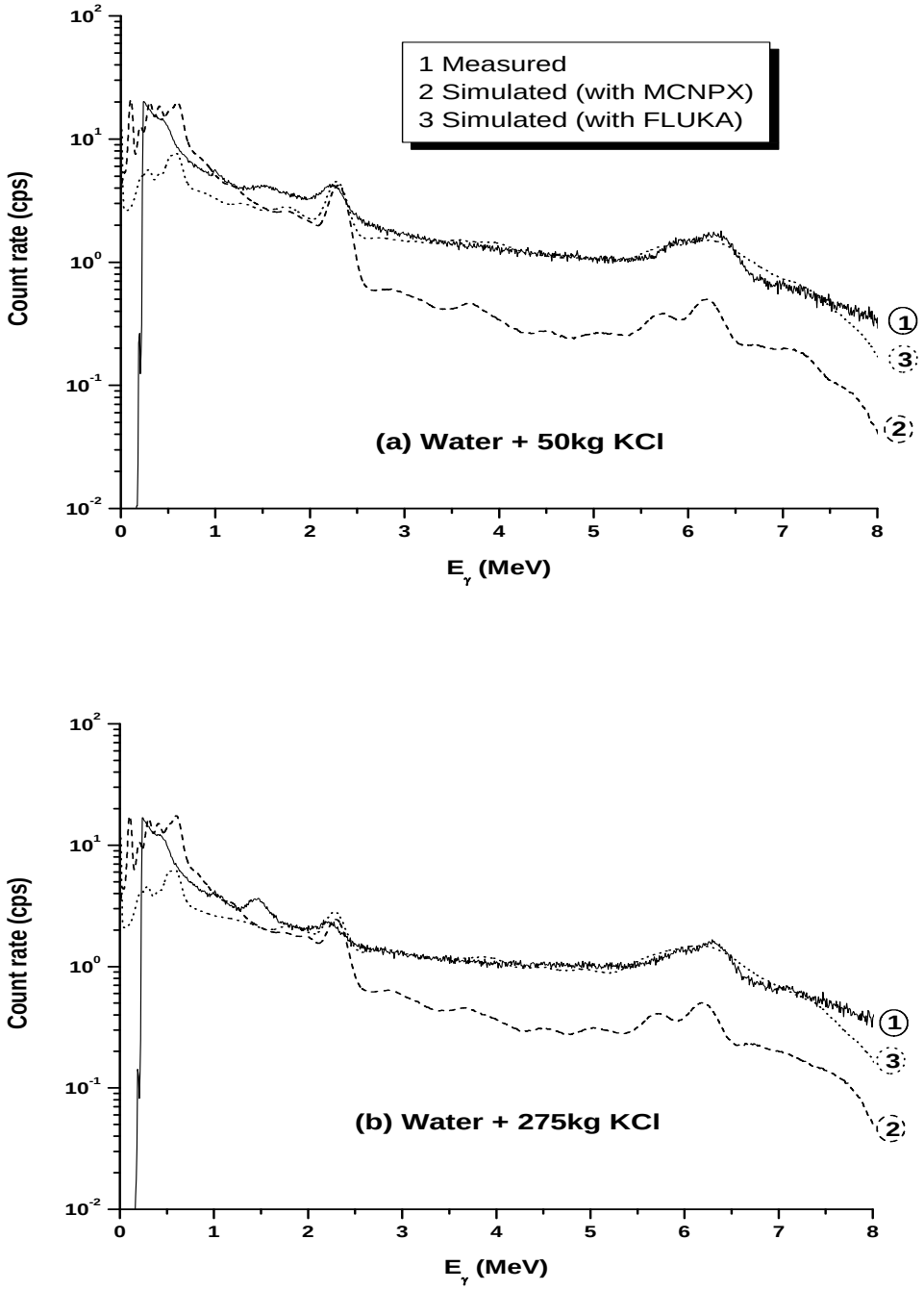

Figure 4.26: *Measured and simulated gamma-ray spectra for water with specified masses of KCl dissolved.*

***Intermezzo 4.3*: Competition for neutron interactions in the concrete tank**

- In intermezzo 4.1, we indicated that the mass of H_2O in the tank is about 6.6×10^3 kg.
- 6.6×10^3 kg of H_2O has about 3.67×10^5 mol of H_2O that is equivalent to about 2.21×10^{29} atoms of H_2O and thus 4.41×10^{29} nuclei of H.
- For each nucleus of H, 99.9% are ^{1}H. This implies that 3.67×10^5 mol of H_2O contains $4.41 \times 10^{29} \times 0.999 \approx$ **4.41×10^{29}** nuclei of ^{1}H.

- Again (intermezzo 4.1) we showed that 1 kg KCl is equivalent to about 8.08×10^{24} atoms of KCl and therefore 8.08×10^{24} nuclei of Cl.
- For each nucleus of Cl, 75.8% are ^{35}Cl. This implies that 13.4 mol of KCl contains $8.08 \times 10^{24} \times 0.758 \approx$ **6.12×10^{24}** nuclei of ^{35}Cl.
- So e.g. a mass of 275 kg of KCl represents **1.68×10^{27}** nuclei of ^{35}Cl.

- As more KCl is added, the number of ^{35}Cl nuclei available for the (n,γ) reaction also increases in direct competition with the ^{1}H(n,γ)^{2}H reaction for the thermal neutrons.
- The rate for a particular nuclear reaction is related to the neutron flux, the microscopic cross section for the interaction and atom density of the target (more details in section 2.4).
- At thermal neutron energies the microscopic cross section: σ(^{35}Cl)= **43.6 b** compared to σ(^{1}H)= **0.33 b** (Firestone, 1996).

So considering the macroscopic cross section at thermal energies in eq. 2.6 ($\Sigma_a = N \cdot \sigma_a$), the product of the number of nuclei density and the microscopic cross section, one obtains $\Sigma_a = 1.11$ and $2.20\ m^{-1}$ for ^{35}Cl and ^{1}H, respectively. Compared to water only, one expects a reduction in intensity for the $E_\gamma = 2.22$ MeV peak by about 1/3 at an added mass of 275 kg KCl.

4.3.2.3 The borehole formation analysis tests

As a continuation of the PNDT-on measurements, the NuPulse instrument was also tested in the KVI borehole. In figure 4.27 we present the neutron-induced gamma-ray spectra acquired at various depth of the borehole. The intensities for the major contributions vary by a factor of 1.5 to 2 depending on depth. The results mainly confirm the presence of water in the borehole and the spectra are little influenced by contributions from other elements. Almost at the top (-2 m), the ^{1}H(n,γ)^{2}H reaction photopeak intensity is about a factor of 2 lower than at deeper levels. For the high-energy region, no major variations are observed. Because of the limited possibility for a quantitative analysis of the borehole measurements, the present NuPulse instrument for the PNDT-on cannot supply sufficient information to interpret the borehole structures.

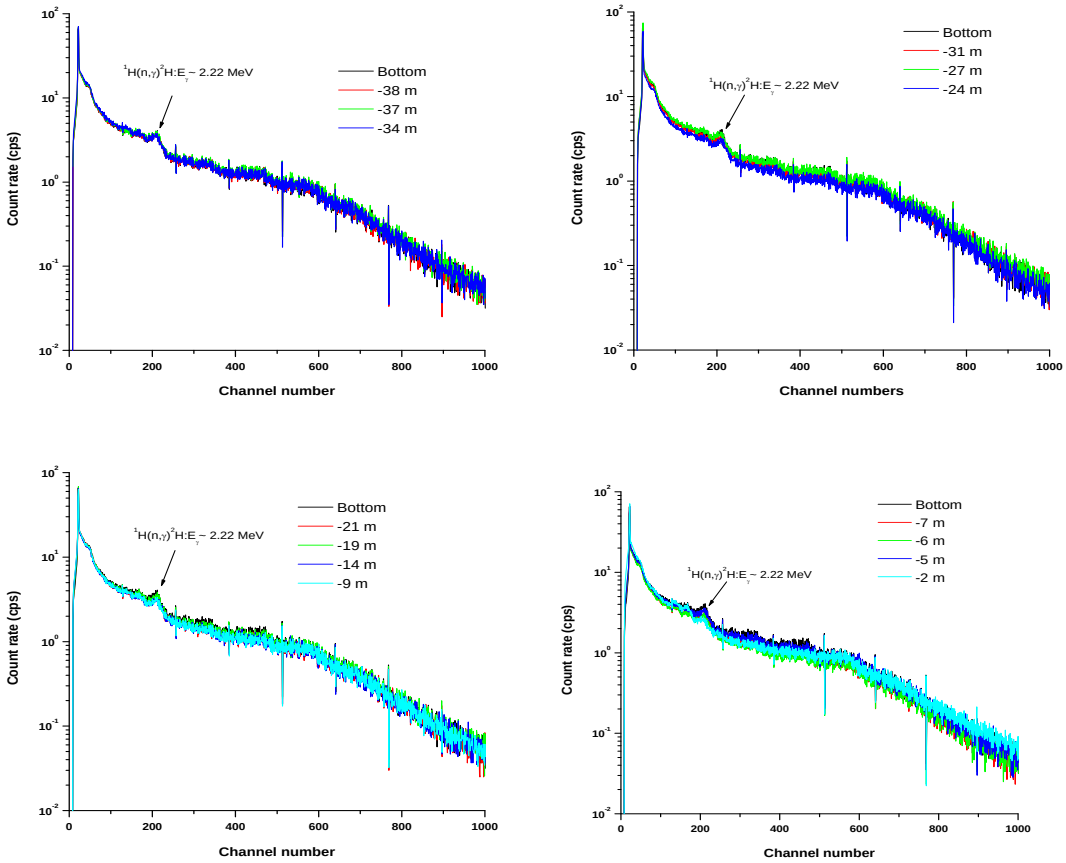

Figure 4.27: *Neutron-induced gamma-ray spectra obtained with NuPulse instrument inside the KVI borehole at various depths from the bottom to the top surface.*

4.4 Conclusion

In this chapter, we have described the gamma-ray spectroscopy with the NuPulse instrument. The results show that more tests and investigations are needed. In the PNDT-off measurements, the results are well understood and the analysis could be classified as successful. As mentioned earlier, an additional approach (hybrid method) in combination with the FSA method could be deployed to assist in the PNDT-off analysis. Simulation results using MCNPX for the PNDT-off setting are consistent and in total agreement with the measured spectra.

With the PNDT-on, we could demonstrate the effective absorption of thermalised neutrons by the addition of KCl. The simulations, however underestimate the effect by a factor two at the maximum load of 275 kg. Inadequate incorporation of the neutron resonance cross sections for Cl is a likely cause. However, major challenges are encountered for the interpretation of the PNDT-on experiments. The most serious one is the fact, that the gamma-ray spectrum of water, the most simple but also quite abundant target material cannot be reproduced by the MCNPX simulations. The simulation results of FLUKA show spectra that better resemble the

measured spectra, but this could partly be related to the broad-energy gamma-ray groups implemented in FLUKA. Moreover, the test with the FLUKA code reveals also the inconsistency in the results as presented in figure 4.23 (also in figure 4.19) for the empty-tank spectra, whereby the expected gamma-ray energy as evident in the measured spectrum is missing. This feature could be caused by the broad energy binning in FLUKA and points to a drawback in this code.

According to Ferrari et al., "The multigroup scheme adopted in FLUKA is reliable and much faster than any possible approach using a continuous cross section" (Ferrari *et al.*, 2005). With less possibility of having continuous or discrete energy cross-section tables available in FLUKA code soon, the intercomparison becomes complex, moreover the multigroup cross sections available in MCNPX are dated (evaluation year) 1987. We note the improved comparison in FLUKA calculations to reproduce the measured spectra as a step to further investigate benchmark experiments with this code.

Unfortunately we have to conclude that until a much better agreement is achieved between the simulated and measured spectra, this technique will have limited use in quantitative analysis of PNDT neutron-activation data.